

Multi-phase gas properties of extremely strong intervening DLAs towards quasars[★]

A. Ranjan^{1,2,3} , R. Srianand³, P. Petitjean¹, G. Shaw⁶, Y.-K. Sheen², S. A. Balashev⁴, N. Gupta³,
C. Ledoux⁵, and K. N. Telikova⁴

¹ Institut d'Astrophysique de Paris, Sorbonne Université & CNRS, 98bis boulevard Arago, 75014 Paris, France
e-mail: adarsh.ranjan@iap.fr

² Korea Astronomy and Space Science Institute, 776, Daedeokdae-ro, Yuseong-gu, Daejeon 34055, Korea

³ Inter-University Centre for Astronomy and Astrophysics, Post Bag 4, Ganeshkhind 411 007, Pune, India

⁴ Ioffe Institute, Politekhnicheskaya 26, 194021 Saint Petersburg, Russia

⁵ European Southern Observatory, Alonso de Córdova 3107, Vitacura, Casilla 19001, Santiago, Chile

⁶ Tata Inst. of Fundamental Research, Homi Bhabha Road, Colaba Mumbai 400005, India

Received 18 February 2021 / Accepted 4 January 2022

ABSTRACT

We present the results of a spectroscopic analysis of extremely strong damped Ly α absorbers (ESDLAs; $\log N(\text{HI}) \geq 21.7$) observed with the medium resolution spectrograph, X-shooter at the Very Large Telescope (VLT). Recent studies in the literature indicate that ESDLAs probe gas from within the star-forming disk of the associated galaxies and thus ESDLAs provide a unique opportunity to study the interstellar medium of galaxies at high redshift. We report column densities (N), equivalent widths (w , for Mg II and Ca II transitions), and the kinematic spread (Δv_{90}) of species from neutral (namely O I, Ar I, Cl I, N I, and Na I), singly ionised (Mg II, Ca II, S II, Ni II, Mn II, Ti II, and P II), and higher ionisation (C IV, Si IV, N V, and O VI) species. We estimate the dust-corrected metallicity measured using different singly ionised gas species such as P II, S II, Si II, Mn II and Cr II, and Zn II. We find that, using the dust correction prescription, the measured metallicities are consistent for all mentioned species in all ESDLAs within 3σ uncertainty. We further perform a quantitative comparison of column densities, equivalent widths, and kinematic spreads of ESDLAs with other samples that are associated with galaxies and detected in absorption along the line of sight towards high-redshift quasars (QSOs). We find that the distributions of the Ar I to H I column density ratio ($N(\text{Ar I})/N(\text{H I})$) in DLAs and ESDLAs are similar. We further report that ESDLAs do not show a strong deficiency of Ar I relative to other α -capture elements as is seen in DLAs. This supports the idea that the mentioned under-abundance of Ar I in DLAs is possibly caused by the presence of background UV photons that penetrate the low $N(\text{H I})$ clouds to ionise Ar I, but they cannot penetrate deep enough in the high $N(\text{H I})$ ESDLA environment. The $w(\text{Mg II}\lambda 2796)$ distribution in ESDLAs is found to be similar to that of metal-rich C I-selected absorbers, but the velocity spread of their Mg II profile is different. The dust content (measured by modelling the quasar extinction) and $w(\text{Ca II}\lambda 3934)$ distributions are similar in ESDLAs and Ca II-selected absorbers, yet we do not see any correlation between $w(\text{Ca II}\lambda 3934)$ and dust content. The Δv_{90} velocity spread of singly ionised species in ESDLAs is statistically smaller than that of DLAs. For higher ionisation species (such as C IV and Si IV) that trace the warm ionised medium, Δv_{90} is similar in the two populations. This suggests that the ESDLAs sample a different H I region of their associated galaxy compared to the general DLA population. We further study the $N(\text{Cl I})$ distribution in high-redshift DLA and ESDLA sightlines, as Cl I is a good tracer of H₂ gas. The $N(\text{Cl I})$ – $N(\text{H}_2)$ correlation is followed by all the clouds (ESDLAs and otherwise) having $\log N(\text{H}_2) < 22$.

Key words. quasars: absorption lines – galaxies: high-redshift – galaxies: ISM

1. Introduction

Damped Ly α absorption systems (DLAs) correspond to a particular class of H I absorption systems, with a H I column density, $\log N(\text{H I})$ (cm^{-2}) ≥ 20.3 ¹ (see e.g., Wolfe et al. 1986). These absorbers can be easily recognised through their damped Ly α absorption feature in the spectra of bright background sources such as quasars (QSOs) and γ -ray bursts (GRBs). Statistically, DLAs have been shown to dominate the neutral gas mass density in the high-redshift universe, providing the primary fuel for star formation (Wolfe et al. 2005; Prochaska et al. 2005; Noterdaeme et al. 2009, 2012a;

Zafar et al. 2013; Crighton et al. 2015; Sánchez-Ramírez et al. 2016). In some cases, DLAs are found to be associated with the halo and/or the circumgalactic medium (CGM) of galaxies at high redshift ($z \sim 2$) (see e.g., Noterdaeme et al. 2012b; Péroux et al. 2012, 2018; Fynbo et al. 2013) as well as low redshifts ($z < 1$) (see e.g., Rahmani et al. 2016, and references therein). Furthermore, an anticorrelation between the H I column density and the impact parameter of the host galaxy, ρ , is observed (see e.g., Pontzen et al. 2008; Noterdaeme et al. 2012b; Rahmati & Schaye 2014; Krogager et al. 2017).

Hence, it is expected that the highest end of the $N(\text{H I})$ distribution can preferentially probe the star-forming disk of the associated galaxies. Following this argument, Noterdaeme et al. (2014) studied ~ 100 extremely strong DLAs (or ESDLAs) defined as systems with H I column density, $\log N(\text{H I}) \geq 21.7$ at high redshift ($z \sim 2$ –4). Stacking the low resolution SDSS

[★] Based on observations performed with the Very Large Telescope of the European Southern Observatory under Prog. ID 095.A-0224(A) and 0101.A-0891(A) using the X-shooter spectrograph.

¹ In the following text, column densities, N , are given in cm^{-2} .

spectra led to the detection of Ly α emission within the SDSS fibres (i.e. within an impact parameter of ~ 8 pc from the quasar sight line at the redshift of the DLAs, i.e. $z \sim 2.5$). Additionally, numerical simulations (e.g., Altay et al. 2013) show that the highest end of the HI column density distribution function is sensitive to the effects of stellar feedback and H₂ formation. Indeed, it is seen in high- z observations that ESDLAs have a significantly enhanced fraction of diffuse H₂ gas observed in comparison with regular DLAs (e.g., Noterdaeme et al. 2015a; Balashev & Noterdaeme 2018).

This motivated a medium spectral resolution, wide wavelength range follow-up study of 11 ESDLAs using the X-shooter spectrograph at the Very Large Telescope (VLT, Paranal, Chile). These ESDLAs were identified using SDSS spectra (Noterdaeme et al. 2014). The analysis of one of these ESDLAs towards SDSS J1513+0352 (see Ranjan et al. 2018) led to the H₂ detection with the highest H₂ column density ever observed in QSO absorption line studies along with Ly α emission detected at a small impact parameter ($\rho = 1.4$ kpc) relative to the quasar line of sight.

The detailed analysis of the initial sample of 11 ESDLAs (along with ESDLAs taken from literature) is presented in Ranjan et al. 2020. The study notes that ESDLAs probe transitioning HI-H₂ gas clouds with much higher frequency ($\sim 50\%$ of the cases have H₂) as compared to the general DLA population, where only 5–10% of the systems are detected with H₂ (Petitjean et al. 2000; Ledoux et al. 2003; Noterdaeme et al. 2008; Balashev & Noterdaeme 2018). They also show that faint emission lines are detected in proximity to the absorbers which indicates that ESDLAs arise from the star-forming disk of their associated galaxy. Although, the direct study of the galaxy morphology is not possible due to the non-detection of the faint stellar continuum of these galaxies. Hence, we need to probe alternative methods to understand the nature of ESDLAs and their associated galaxies. The galaxies associated with ESDLAs are detected independently of their intrinsic luminosity. In Ranjan et al. (2020), we focus primarily on the H₂ detection and the proximity of ESDLAs with their associated galaxy. In this paper, we intend to gain additional information about the physical and chemical properties of ESDLAs and the associated galaxies by studying the absorption lines of neutral (such as C I and Ar I), singly ionised (such as Mg II and Ca II), as well as highly ionised (such as C IV, Si IV, N V, and O VI) gas species. The comprehensive study probes features of gas in different ionisation states that are associated with the ESDLA host galaxy. We calculated the column density (and/or the equivalent width in specific cases) and quantified the gas kinematics (using Δv_{90} , defined as the velocity interval that contains 90% of the area under the apparent optical depth spectrum) of differently ionised species. We study the distribution of column density and velocity spread of gas species in different ionisation states and further compare them to other DLA sub-sets associated with galaxies such as the metal-rich C I-selected absorbers (see e.g., Ledoux et al. 2015; Zou et al. 2018; Noterdaeme et al. 2018), dust rich DLAs selected based on their Ca II equivalent width (see e.g., Wild & Hewett 2005), Mg II-selected strong absorbers (see e.g., Rao et al. 2005), and absorbers associated with outflowing gas clouds (see e.g., Fox et al. 2007, 2008). The comparison will help us to further understand the ESDLA gas clouds and their associated galaxies.

Details of the observations and data reduction are presented in Sect. 2. The analysis of the absorption lines is described in Sect. 3. The results of our study are presented in Sect. 4 and discussed in Sect. 5. In Sect. 6 we summarise our findings.

2. Observations and data reduction

Here, we use a sample of 11 ESDLAs observed with the VLT/X-shooter spectrograph. Spectra of 11 quasars from the first programme (ESO programme ID 095.A-0224(A)) were analysed in Ranjan et al. (2020, 2018). The observations were carried out in service mode under good seeing conditions (typically 0.7–0.8'') between April 2015 and July 2016 with the multiwavelength medium-resolution spectrograph X-shooter (Vernet et al. 2011) mounted at the Cassegrain focus of the Very Large Telescope (VLT-UT2) at Paranal, Chile. A two-step nodding mode with an offset of 4 arcsec between the two integrations was used. We reduced the data using the standard X-shooter pipeline (Modigliani et al. 2010) and combined individual exposures by weighting the measured flux in each pixel by the inverse of its variance to obtain the combined 2D and 1D spectra. The target spectra were obtained at medium spectral resolution, $R \sim 5000$ – $10\,000$, depending on the arm of the spectrograph corresponding to the typical width of the instrument function, $FWHM \sim 30$ – 60 km s⁻¹. We found that the resolution in most of the individual spectra are seeing-dominated. The detailed list of resolution for individual spectra can be found in Ranjan et al. (2020). For the absorption line analysis presented here, we have only used the combined 1D spectra of each arm of the X-shooter spectrograph. Further details about the observations and data reduction can be found in Ranjan et al. (2020). The long form QSO names (with precise RA, Dec information) with the QSO and the absorbers' redshifts are given in Table 1. Throughout this paper, we use a short notation for the quasar names, for example SDSS J 223250.98+124225.29 is referred to as J2232+1242.

We additionally use information about seven new ESDLAs observed with VLT X-shooter using similar observing conditions from Telikova et al. (2022) (initially discussed in Telikova et al. 2020). We further add information about five ESDLAs from literature, found towards the QSOs HE0027–1836 (from Noterdaeme et al. 2007), J0843+0221 (from Balashev et al. 2017), J113–0010 (from Noterdaeme et al. 2012a), and J0230–0334 and Q0743+1421 (from Kulkarni et al. 2015). These ESDLAs form a part of the high- z ESDLA sample that meets the $N(\text{HI})$ criterion and were observed using medium and/or high resolution spectrographs.

3. Absorption-line analysis

We used multi-component Voigt-profile fitting to derive column densities from absorption features. The fitting was performed using VPFIT² (Carswell & Webb 2014). The VPFIT website³ also provides a data file for the atomic parameters that was compiled primarily from Morton 2003, but taking updated references from many other works in the literature (such as Petitjean & Aracil 2004; Abgrall & Roueff 2006; Salumbides et al. 2006; Ivanov et al. 2008; Baillya et al. 2010; Berengut et al. 2011). We primarily used the atomic parameters from this data file for our fitting along with the others mentioned directly in the text.

The initial fit for C I and singly ionised species for the ESDLA sample was reported in Ranjan et al. (2018, 2020). We took advantage of the wide wavelength range of X-shooter spectra to include many transition lines of Fe II and Si II, such as 'Si II λ 1193 ([Å]⁴)', 'Si II λ 1304', 'Si II λ 1526', 'Si II λ 1808',

² <https://www.ast.cam.ac.uk/~rfc/vpfit>

³ <https://www.ast.cam.ac.uk/~rfc/vpfit>

⁴ All wavelengths in this article are given in terms of Å unless specified otherwise.

Table 1. Quasar name, redshift of the quasar (z_{QSO}), redshift of the ESDLA (z_{abs}), column density (in logscale) of H I and H₂, dust content measured in the ESDLA ($E(B - V)$), metallicity relative to solar (in $[M/H]$, where M represents the most undepleted neutral gas species), Δv_{90} , $\Delta v_{90}(\text{C IV})$, and column density (in logscale) of Si II for ESDLAs.

Quasar	z_{QSO}	z_{abs}	$N(\text{H I})$	$N(\text{H}_2)$	$E(B - V)$	$[M/H]$	Δv_{90}	$\Delta v_{90}(\text{C IV})$	$N(\text{Si II})$
SDSS J001743.8+130739.8	2.594	2.326	21.62 ± 0.03	<18.3	0.11	-1.5 ± 0.09	120	430	16.01 ± 0.13
SDSS J002503.0+114547.8	2.961	2.304	21.92 ± 0.09	~ 20	0.19	-0.53 ± 0.11	240	–	$16.67 - 17.18^{(a)}$
SDSS J114347.2+142021.6	2.583	2.323	21.64 ± 0.06	18.3 ± 0.1	0.08	-0.8 ± 0.06	130	–	16.30 ± 0.03
SDSS J125855.4+121250.2	3.055	2.444	21.9 ± 0.03	<18.3	0.02	-1.43 ± 0.04	100	270	16.10 ± 0.04
SDSS J134910.4+044819.9	3.353	2.482	21.8 ± 0.01	<18.1	0.03	-1.35 ± 0.06	60	–	$16.47 - 17.24^{(a)}$
SDSS J141120.5+122935.9	2.713	2.545	21.83 ± 0.03	<15.9	0.03	-1.59 ± 0.08	50	220	16.07 ± 0.18
SDSS J151349.5+035211.6	2.68	2.464	21.83 ± 0.01	21.31 ± 0.01	0.13	-0.84 ± 0.23	90	200	16.92 ± 0.24
SDSS J214043.0–032139.2	2.479	2.339	22.41 ± 0.03	20.13 ± 0.07	0.04	-1.52 ± 0.08	70	–	$16.04 - 17.31^{(a)}$
SDSS J223251.0+124225.3	2.299	2.23	21.75 ± 0.03	18.56 ± 0.02	0.004	-1.48 ± 0.05	75	320	$15.69 - 17.23^{(a)}$
SDSS J224621.1+132821.3	2.514	2.215	21.73 ± 0.03	<16.3	<0.004	-1.84 ± 0.1	65	230	15.63 ± 0.21
SDSS J232207.3+003349.0	2.693	2.477	21.58 ± 0.03	<16.0	<0.004	-1.71 ± 0.13	40	140	15.47 ± 0.06

Notes. Δv_{90} is derived from unsaturated transitions of singly ionised species, such as Ni II and Zn II. All data are taken from Ranjan et al. (2020) (and references therein), except for $\Delta v_{90}(\text{C IV})$ and $N(\text{Si II})$, which is calculated in this work. ^(a)Taking into account the effects of saturation and blends, we provide revised estimates of $N(\text{Si II})$ here. See Sect. 4.8 for discussion.

‘Fe II $\lambda 1608$ ’, ‘Fe II $\lambda 1611$ ’, ‘Fe II $\lambda 2249$ ’, ‘Fe II $\lambda 2260$ ’, ‘Fe II $\lambda 2344$ ’, ‘Fe II $\lambda 2374$ ’, ‘Fe II $\lambda 2382$ ’, ‘Fe II $\lambda 2586$ ’, and ‘Fe II $\lambda 2600$ ’. Using so many transitions with varying oscillator strengths⁵ is advantageous as it helps in resolving the highest number of low column density sub-components (in transitions with strong absorption) that can be identified separately given the spectral resolution. In addition, we can also constrain the column density for sub-components that appear saturated in transitions with a strong absorption signature by looking at the transitions with a weaker absorption signature. Hence, fitting a multi-component absorption model for all transitions mentioned above (in addition to other transitions from Cr II, Zn II, Mg I, Ni II, and Ti II) with their b -values and redshifts tied together helps us obtain a robust estimate on the total column density of the mentioned species for these ESDLAs. For Ca II, we report the total column density as well rest-frame equivalent width (w) for its two prominent transitions, ‘Ca II $\lambda 3934$ ’ and ‘Ca II $\lambda 3969$ ’. The Mg II profiles (‘Mg II $\lambda 2796$ ’ and ‘Mg II $\lambda 2803$ ’) are strongly saturated. Hence, we report only the rest-frame equivalent width (w) for both the transitions. We applied a similar fitting approach for higher ionisation species, such as Si IV, C IV, and N V (i.e. tying the b -values and redshifts for multiple transitions of the mentioned ionisation), but the fitting was performed separately from that of the low-ionisation species. We found that the redshifts for individual components derived from fitting the higher ionisation lines (C IV, Si IV, and N V) are only slightly separated in velocity space ($\lesssim 50 \text{ km s}^{-1}$) from the components of the lower ionisation lines.

4. Results

In Ranjan et al. (2020), we studied only C I and singly ionised species (e.g., Fe II, Zn II, and Si II) and the H I–H₂ transition for 11 ESDLAs mentioned in Table 1. The table shows basic information about the 11 ESDLAs from Ranjan et al. (2020) for reference that is used for this study. In continuation, we further searched for and analysed the following neutral gas species: oxygen (O I), argon (Ar I), nitrogen (N I), chlorine (Cl I), sodium (Na I), singly ionised calcium (Ca II), sulphur (S II),

⁵ Transitions with high oscillator strength produce strong absorption signature that might sometimes be intrinsically saturated depending of the sub-component column density, yet they might be unsaturated in transitions with lower oscillator strength.

magnesium (Mg II), phosphorous (P II), titanium (Ti II), manganese (Mn II), nickel (Ni II), and four higher ionisation species – carbon (C IV), silicon (Si IV), nitrogen (N V), and oxygen (O VI). The results of our analysis (column density, rest-frame equivalent width, and Δv_{90} estimates) for 11 ESDLAs are provided in Table 2 and Table A.1. Table 2 also provides additional information about the seven ESDLAs studied in detail in Telikova et al. (2022). We provide important details for each species in the following subsections.

In addition to these, we also use the relevant ESDLAs data from literature. They include the following: Noterdaeme et al. (2007), towards QSO HE0027–1836, with $\log N(\text{Ar I}) = 14.42 \pm 0.02$, $\log N(\text{H I}) = 21.75 \pm 0.1$, and $\log N(\text{H}_2) = 17.3 \pm 0.07$; Noterdaeme et al. (2012a), towards QSO J1135–0010, with $w(\text{Mg II } \lambda 2796) = 3.6 \text{ \AA}$, and $\log N(\text{H I}) = 22.1 \pm 0.05$; Balashev et al. (2017), towards QSO J0843+0221, with $\log N(\text{Cl I}) = 13.63^{+0.20}_{-0.05}$, $\log N(\text{H I}) = 21.82 \pm 0.11$, and $\log N(\text{H}_2) = 21.21 \pm 0.02$; and Kulkarni et al. (2015), towards QSO J0230–0334, with $\log N(\text{H I}) = 21.74 \pm 0.1$, $\log N(\text{C IV}) = 14.6 \pm 0.05$, and $\log N(\text{Si IV}) = 13.89 \pm 0.04$ as well as towards QSO Q0743+1421, with $\log N(\text{H I}) = 21.9 \pm 0.1$, $\log N(\text{C IV}) = 14.41 \pm 0.07$, and $\log N(\text{Si IV}) = 13.84 \pm 0.06$.

4.1. Neutral oxygen

Neutral oxygen absorption is present in all ESDLAs in our sample. We primarily used the ‘O I $\lambda 1302$ ’ transition to estimate the O I column density. We also used the ‘O I $\lambda 1039$ ’ line wherever possible, but with extreme caution as this transition is inside the Ly α forest and can also be blended with H₂ lines. Since our study is related to gas associated with galaxies, there is a chance that O I column densities are high and hence, most of the ‘O I $\lambda 1302$ ’ lines are probably visibly or intrinsically saturated (a situation where the convolved absorption profile appears to be unsaturated, but the true unconvolved profile is saturated). Since our spectra are of medium resolution, the convolved absorption profile may appear unsaturated in many cases, when the true unconvolved profile is indeed saturated. In such cases, there is a degeneracy between the b -value and column density, and in the absence of additional information, the column density estimate might not be robust.

Therefore, we used the ‘O I $\lambda 1302$ ’ profile taking component information (redshift and b -value) from other singly ionised species (such as Fe II and Zn II) to report a lower

Table 2. Column density (in logscale) of gas species, O I, Ar I, Cl I, Si IV, and C IV, the absorber rest-frame equivalent width (w in Å) of ‘Ca II λ 3934’ and ‘Mg II λ 2796’ lines, and the velocity spread, Δv (in km s $^{-1}$) of the ‘Mg II λ 2796’ line for ESDLAs.

QSO	$N(\text{O I})$	$N(\text{Ar I})$	$N(\text{Cl I})$	$N(\text{Si IV})$	$N(\text{C IV})$	$w(\text{Ca II}\lambda 3934)$	$w(\text{Mg II}\lambda 2796)$	$\Delta v(\text{Mg II})^{(b)}$
J0017+1307	>17.0	14.72 ± 0.19	<12.55	13.38 ± 0.23	14.02 ± 0.22	<0.57	1.88 ± 0.01	190
J0025+1145	>18.6	–	13.5–15.5	>14.19	>14.71	0.7 ± 0.02	4.36 ± 0.01	390
J1143+1420	>18	<15.2	<12.68	>14.02	>14.63	<1.09	3.23 ± 0.02	450
J1258+1212	>17	–	<12.91	13.57 ± 0.08	14.28 ± 0.03	<0.23	2.52 ± 0.02	190
J1349+0448	>16.6	–	–	–	>14.38	0.43 ± 0.14	1.80 ± 0.06	160
J1411+1229	>17.1	~14.4	<12.66	13.45 ± 0.05	13.47 ± 0.1	0.78 ± 0.07	0.95 ± 0.07	110
J1513+0352	>17	–	14.63 ± 0.74	13.65 ± 0.32	14.12 ± 0.32	0.15 ± 0.05	2.89 ± 0.04	340
J2140–0321	18.01 ± 0.18 ^(a)	<15.7	13.37 ± 0.07 ^(a)	>14.06	>14.63	0.26 ± 0.03	1.19 ± 0.02	150
J2232+1242	>16.7	14.43 ± 0.14	<12.72	13.4 ± 0.02	13.8 ± 0.04	0.34 ± 0.04	2.31 ± 0.01	200
J2246+1328	>16.8	14.15 ± 0.32	<12.85	13.48 ± 0.08	14.28 ± 0.19	0.60 ± 0.07	0.77 ± 0.01	100
J2322+0033	>15.7	14.46 ± 0.21	<12.72	13.36 ± 0.05	13.84 ± 0.04	<4.24	1.68 ± 0.06	150
J0024–0725	>17.6	~14.07	<13.25	–	–	0.29 ± 0.07	1.38 ± 0.20	110
J1238+1620	–	~14.69	<13.44	–	–	–	3.94 ± 0.07	290
J1353+0956	>16.7	<14.46	<12.61	–	–	<0.05	1.47 ± 0.18	200
J1418+0718	>16.7	<14.41	<12.22	–	–	–	<0.97	90
J2205+1021	–	~15.25	<13.63	–	–	0.31 ± 0.08	2.63 ± 0.07	210
J2351–0639	–	–	<13.19	–	–	–	1.47 ± 0.17	130
J2359+1354	–	–	<14.13	–	–	0.79 ± 0.11	5.63 ± 0.02	380

Notes. Values starting with ~ represent detections deemed tentative due to either strong blends with sky lines, low signal-to-noise, and/or contamination from the Ly α forest. The estimates for seven additional ESDLAs presented in the bottom of the table demarcated by the horizontal lines are from [Telikova et al. \(2022\)](#). ^(a)Robust estimate for exceptionally high value of $N(\text{O I})$ measured by comparing X-shooter spectra with high resolution UVES spectra (studied in [Noterdaeme et al. 2015b](#)). The UVES spectra were also used to measure $N(\text{Cl I})$. ^(b) Δv was obtained here for saturated ‘Mg II λ 2796’ profiles, and it is defined as the velocity separation between the two extreme pixels where the optical depth $\tau < 0.1$ (see [Zou et al. 2018](#), for detailed discussion). We note that this is different from the standard Δv_{90} measurement of unsaturated lines.

limit for the O I column density in all ESDLAs, except for the $z_{\text{abs}} = 2.339$ system towards QSO J2140–0321. We obtained a $\log N(\text{O I}) = 18.01 \pm 0.18$ for this ESDLA. [Noterdaeme et al. \(2015b\)](#) have also published the results for this ESDLA using spectra obtained with the high resolution Ultraviolet and Visual Echelle (VLT-UVES, $R \sim 48\,000$) spectrograph. We further cross-checked our measured values for column densities with [Noterdaeme et al. \(2015b\)](#). Our estimates match with theirs ($\log N(\text{O I}) = 17.9 \pm 0.2$) within the measured uncertainties. However, we note that this robust estimate from single X-shooter spectra may not be representative of the sample. The column density estimates for O I are listed in Table 2.

We also searched for the presence of absorption from the fine-structure transition of O I. In only one case, that is for ESDLA towards QSO J2140–0321, are we able to confirm the detection of O I* absorption that is well separated from the Si II λ 1304 line and measure $\log N(\text{O I}^*) = 13.82 \pm 0.10$. This is consistent with that measured by [Noterdaeme et al. \(2015a\)](#) using the UVES spectrum. There is a 2σ detection in the case of the ESDLA towards J1411+1228. For the ESDLA towards QSO J2232+1242, the O I* λ 1304 absorption is blended with the Si II λ 1304 line ($\log N(\text{O I}^*) = 13.46 \pm 0.19$). In the remaining cases, we do not have a clear detection at more than the 3σ level. The $N(\text{O I}^*)$ upper limits ($X\sigma$ level) estimated from the non-detection of the $\lambda = 1304$ line for all other ESDLAs are listed in Table A.1.

4.2. Neutral argon

Neutral argon is difficult to probe in high- z clouds especially because the twin transitions – ‘Ar I λ 1066’ and ‘Ar I λ 1048’ are located within the Ly α forest. We fitted these transitions together taking any possible contamination from intervening Ly α absorption into account and using the same component structure as other low ionisation species such as Fe II and Zn II. We estimated the column density of Ar I in four of our ESDLAs,

towards the QSOs J0017+1307, J2232+1242, J2246+1328, and J2322+0033. For the ESDLA towards QSO J1411+1229, we could only fit the ‘Ar I λ 1066’ line and hence, we consider this detection as tentative. For the system towards QSO J2140–0321, the Ar I transitions are blended strongly with the Ly α forest. Hence, we used our X-shooter spectra in combination with the high-resolution UVES spectra to obtain a tentative upper limit estimate on the column density. We intend to use these tentative estimates in our discussion as the component structure (redshift and b -value) used is consistent with that of lines from other low-ionisation species (such as Fe II and Zn II). Apart from this, we have a system towards QSO J1143+1420, for which the Ar I transition is too weak to be considered a confirmed detection. For this system, we obtained a 3σ upper limit on the column density. The column density for all detections and upper limits are listed in Table 2. In Fig. 1, we compare our distribution of the $N(\text{Ar I})/N(\text{H I})$ ratio in ESDLAs with that of the general DLA population studied by [Zafar et al. \(2014\)](#). Based on the Kolmogorov–Smirnov test (K-S test) p -value of 0.9 between ESDLAs from this work and DLAs from [Zafar et al. \(2014\)](#), we can argue that the distribution of a neutral argon abundance in DLAs and ESDLAs are indistinguishable.

4.3. Neutral chlorine

Due to efficient charge exchange reactions between Cl I and H $_2$ (see for e.g., [Jura 1974](#)), chlorine is predominantly neutral in the presence of H $_2$. [Balashev et al. \(2015\)](#) also noted a strong association of neutral chlorine with H $_2$ gas in high- z absorbers. [Ranjan et al. \(2020\)](#) found diffuse H $_2$ signatures in their rest-frame Lyman-Werner (L-W) band absorption in about ~50% of the ESDLAs. Although, the Ly α forest at high redshift is dense enough to create strong blends with the L-W band and create confusion. In addition, there are cases (such as the ESDLA towards QSO J0025+1145), where the L-W band signatures are washed away due to the presence of a Lyman-limit

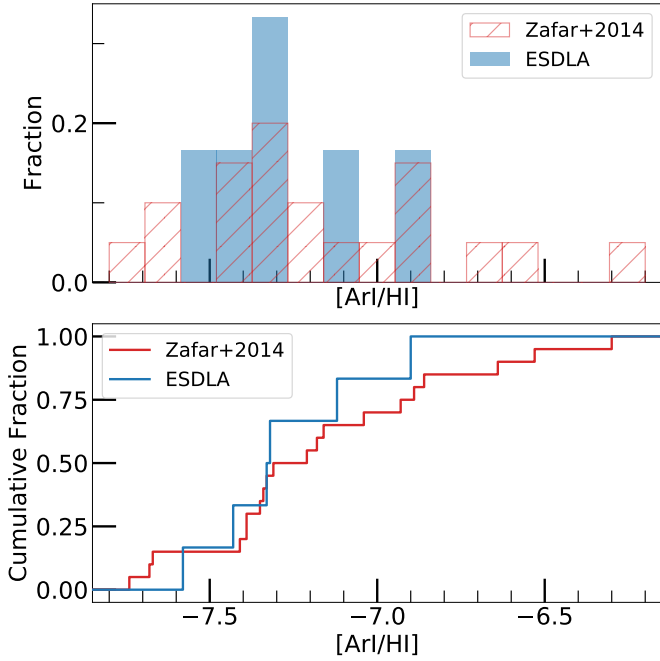


Fig. 1. Distributions of the column density ratio, $N(\text{ArI})/N(\text{HI})$, in ESDLAs (blue curves, this work) and the general DLA population (red curves, Zafar et al. 2014). The histogram and cumulative distributions from the two samples are compared in the *top* and *bottom* panels, respectively.

system. Hence, tracers such as C I and C II can be used as indirect evidence for the presence of H_2 gas. Thus, we would like to study the presence of C II in our sample.

We primarily looked for C II transitions at $\lambda = 1347 \text{ \AA}$ and $\lambda = 1363 \text{ \AA}$ (atomic data taken from Schectman et al. 1993) and the transitions at $\lambda = 1335 \text{ \AA}$, $\lambda = 1379 \text{ \AA}$, and $\lambda = 1389 \text{ \AA}$ (atomic data taken from Welty et al. 2020, and references therein). Other C II transitions located in the Ly α forest (such as C II transitions at $\lambda = 1088 \text{ \AA}$, $\lambda = 1188 \text{ \AA}$, and $\lambda = 1084 \text{ \AA}$, reported in Oliveira & Hébrard 2006, and references therein) have a high probability of being blended with other absorption lines. We note the non-detection of ‘C II $\lambda 1363$ ’ in all our spectra. We also note that the transition ‘C II $\lambda 1335$ ’ is heavily blended with the saturated ‘C II $\lambda 1334$ ’ and ‘C II* $\lambda 1335$ ’ transitions. Using the other three transitions (at $\lambda = 1347 \text{ \AA}$, $\lambda = 1379 \text{ \AA}$, and $\lambda = 1389 \text{ \AA}$), we fitted the C II lines with the component structure (redshift and b -value) tied with C I, as neutral carbon is also found in the presence of H_2 gas. We note that for two ESDLAs towards QSO J0025+1145 and J1513+0352, the C II $\lambda = 1347 \text{ \AA}$ profile has contamination from other absorbers in proximity. For ESDLAs towards QSO J1513+0352, the other two C II transitions are clear and the contamination near $\lambda = 1347 \text{ \AA}$ is identified. Hence, we get a robust estimate on $N(\text{C II})$. For ESDLAs towards QSO J0025+1145, the other transitions are also contaminated and the $N(\text{C II})$ is highly uncertain. We report the $N(\text{C II})$ lower limit from the $\lambda = 1347 \text{ \AA}$ transition and the upper limit from the $\lambda = 1389 \text{ \AA}$ transition. We also report the robust measurement of $N(\text{C II})$ in ESDLA towards QSO J2140–0321 by combining our medium resolution X-shooter spectra and high-resolution UVES spectra (initially studied in Noterdaeme et al. 2015a). All measurements and upper limits are reported in Table 2.

We detected C II in all systems where H_2 was previously detected. In the new ESDLA sample studied in Telikova et al. (2022), they detected H_2 towards J2205+1021 and J2359+1354. We note that C II is not detected in these systems. Although, the $N(\text{H}_2)$ in these two systems are much lower than the other ESDLAs with confirmed C II detection. Since $N(\text{H}_2) - N(\text{C II})$ are correlated, the non-detection could just indicate the C II detection limit with an X-shooter wavelength range and resolution. The detection of H_2 towards J0025+1145 was declared as tentative in Ranjan et al. (2020) despite a high inferred column density. The reason being the presence of a Lyman-limit system towards QSO J0025+1145 which implies that we could detect only one L-W band of H_2 in that system. The presence of neutral chlorine in this system confirms our previous claim. We report 3σ upper limits on the C II column density for the rest of the ESDLAs, except for ESDLA towards QSO J1349+0448. For this system, all C II transitions are strongly blended.

4.4. Neutral nitrogen

nitrogen is produced in different stages of hydrogen and helium burning shells in stars. There is large uncertainty in the contribution of nitrogen production from different stages in various types of stars such as low, intermediate, or massive stars (see Meynet & Maeder 2002). The study of nitrogen abundance in neutral gas clouds gives important insight into resolving this uncertainty (see e.g., Petitjean et al. 2008). Hence, we looked for neutral nitrogen (NI) in our ESDLA sample as well. We note that NI is another challenging species to detect as its transitions fall within the Ly α forest. However, due to multiple transitions (centred around rest frame $\lambda = 1134 \text{ \AA}$ and $\lambda = 1200 \text{ \AA}$), we were able to detect neutral nitrogen in ESDLAs. In our sample, we report the detection of neutral nitrogen in four ESDLAs towards QSOs J0017+1307, J1411+1229, J2140–0321, and J2232+1242. For the rest of the ESDLAs, the NI profile was either too weak or heavily contaminated with forest lines to be detected robustly in our medium resolution study. The measured column densities and $3\text{-}\sigma$ upper limits are reported in Table A.1.

4.5. Mg II

The Mg II absorption signature has been a common feature of gas associated with galaxies both in the local (see e.g., Bergeron & Boissé 1991; Steidel & Sargent 1992; Feltre et al. 2018) and distant (see e.g., Bouché et al. 2004, 2007; Rao et al. 2005) universe. We detect Mg II absorption in all of our ESDLAs. We note that Mg II is quite abundant in strong HI absorbers (DLAs). The primary transitions, ‘Mg II $\lambda 2796$ ’ and ‘Mg II $\lambda 2803$ ’, are strongly saturated in most DLAs. Hence we report the equivalent width of the mentioned Mg II transitions as previously done in the literature (see e.g., Zou et al. 2018; Matejek et al. 2013). We compare our distribution of ‘Mg II $\lambda 2796$ ’ equivalent widths in ESDLAs (median – 2.1 \AA) with that of other high- z absorption selected samples associated with galaxies, such as the DLA population (taken from Mg II-selected absorbers studied in Matejek et al. 2013, median – 1.72 \AA), the C I-selected high metallicity absorber sample (see, Zou et al. 2018, median – 2.89 \AA), and the Ca II-selected dusty absorber sample (see, Wild & Hewett 2005, median – 2.27 \AA).

Figure 2 shows the distributions of $w(\text{Mg II } \lambda 2796)$ in the above-mentioned samples. The K-S test reveals that the Mg II equivalent width distribution of ESDLAs. ESDLAs are indistinguishable from that of the Mg II-selected DLA population

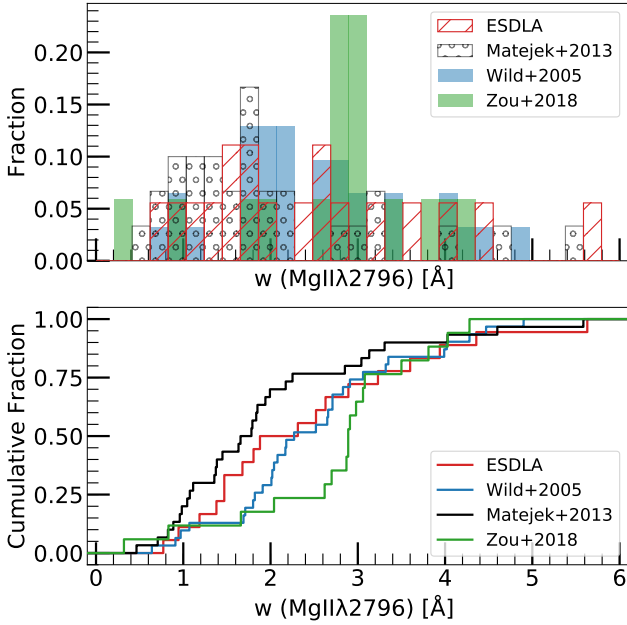


Fig. 2. $w(\text{Mg II}\lambda 2796)$ in different samples. *Top panel:* distribution of the ‘Mg II $\lambda 2796$ ’ equivalent width (w) in the ESDLAs (red hashed histogram, this work), CI-selected absorbers (green filled histogram, from Zou et al. 2018), Ca II-selected absorbers (blue filled histogram, from Wild & Hewett 2005), and the general DLA population (grey dotted histogram, from Matejek et al. 2013). *Bottom panel:* cumulative distributions of the same samples using the same colours.

(p -value = 0.35). ESDLAs also tend to have $w(\text{Mg II}\lambda 2796)$ similar to the Ca II-selected sample as testified by the medians of the samples. The K-S test of ESDLAs with the Ca II sample (p -value = 0.37) also indicates that the sample distributions are indistinguishable. We performed a K-S test with the CI-selected sample as well and found that the samples are consistent with being drawn from the same parent population (p -value = 0.13). In addition, we show the different samples mentioned above in the $N(\text{H I}) - w(\text{Mg II}\lambda 2796)$ plane in Fig. 3. We note that the $N(\text{H I})$ for ESDLAs and $w(\text{Mg II}\lambda 2796)$ for the Matejek et al. (2013) sample are restricted by their respective selection technique. Although, we note that the $w(\text{Mg II}\lambda 2796)$ for the sample of ESDLAs is quite varied and no significant relation can be drawn between the two quantities shown in the figure.

In addition to the Mg II equivalent width, we also report the velocity spread of Mg II absorption using $\Delta v(\text{Mg II}\lambda 2796)$ similar to Zou et al. (2018) in Table 2. In their paper, Zou et al. (2018) define Δv as the velocity separation between the two extreme pixels where the optical depth $\tau < 0.1$. We note that the velocity spread of ESDLAs is different (K-S test p -value = 0.02) and statistically smaller (median = 150 km s^{-1}) than that of the CI-selected absorbers (median = 390 km s^{-1})⁶.

4.6. Na I and Ca II

With an ionisation potential of 5.1 eV, neutral sodium (Na I) serves as a tracer for cold neutral gas (see Crawford 1992). We did not find any significant trace of Na I in our sample. The stronger transitions on Na I lie in the far end of the X-shooter near-infrared (NIR) arm (rest wavelengths 5891 Å and 5897 Å),

⁶ The velocity spread of ‘Mg II $\lambda 2796$ ’ in CI-selected absorbers was obtained with private communication from the authors of Zou et al. (2018).

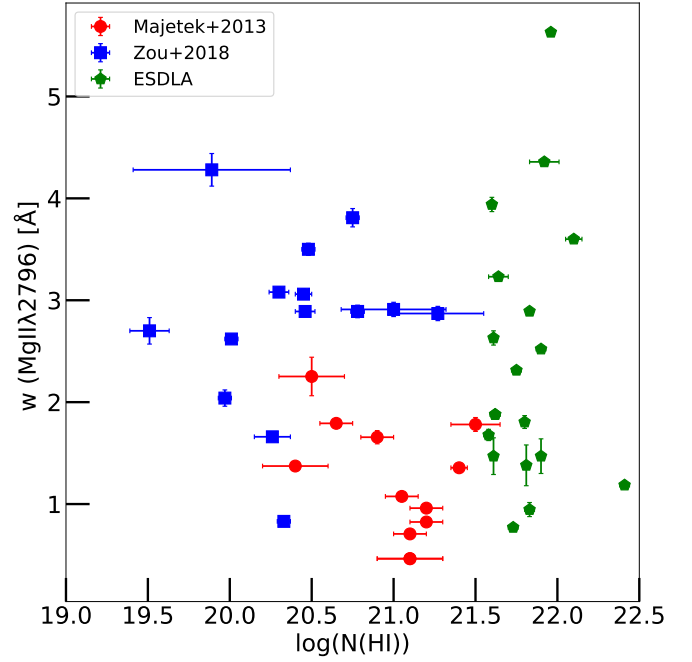


Fig. 3. $\log N(\text{H I})$ [atoms cm^{-2}] vs. $w(\text{Mg II}\lambda 2796)$ [Å] for ESDLAs (green points, this work), CI-selected absorbers (blue points, from Zou et al. 2018), and the Mg II-selected population of DLAs (red points, from Matejek et al. 2013).

where the signal-to-noise ratio (S/N) is very poor in our observations. Hence, we note that the non-detection in our observations is not necessarily an indication of a low abundance of Na I. In Table A.1, we report the 3σ upper limit on the column density of Na I in our sample.

A Ca II absorption signature has been associated with dusty DLAs at high redshift (see e.g., Wild et al. 2006; Nestor et al. 2008). We found signatures of Ca II absorption in seven ESDLAs. For weak transitions, we calculated the equivalent width (w) of the absorption profile. In cases where the spectra have a low S/N, we checked whether the value for the equivalent width is greater than a 3σ uncertainty and we report it as detection if this is true. If not, we used the Voigt profile model to estimate a 3σ upper limit on the column density. The NIR spectrum has significant sky residuals hindering a robust estimate of the equivalent width of some transitions such as ‘Ca II $\lambda 3934$ ’ and ‘Ca II $\lambda 3969$ ’. For systems towards QSO J1513+0352 and J2246+1328, the respective transitions, ‘Ca II $\lambda 3934$ ’ and ‘Ca II $\lambda 3969$ ’, are contaminated. Hence, we declare them to be tentative in our list. In Table A.1, we report the column density of Ca II in our sample. Additionally, in Table 2, we report the equivalent width of the ‘Ca II $\lambda 3934$ ’ transition as this has been previously used in the literature.

Figure 4 shows the distribution of $w(\text{Ca II}\lambda 3934)$ (left) and $E(B - V)$ (right) for ESDLAs in our sample, CI-selected absorbers from Zou et al. (2018), and the Ca II-selected sample from Wild & Hewett (2005). The $E(B - V)$ for ESDLAs were obtained from Ranjan et al. (2020). K-S tests between ESDLAs and CI-selected absorbers for $w(\text{Ca II}\lambda 3934)$ (p -value = 0.79) and $E(B - V)$ (p -value = 0.18) and with the Ca II-selected absorber sample, with a p -value = 0.31 for $w(\text{Ca II}\lambda 3934)$ and a p -value = 0.41 for $E(B - V)$ indicate that the dust content and Ca II abundance for all three samples are indistinguishable.

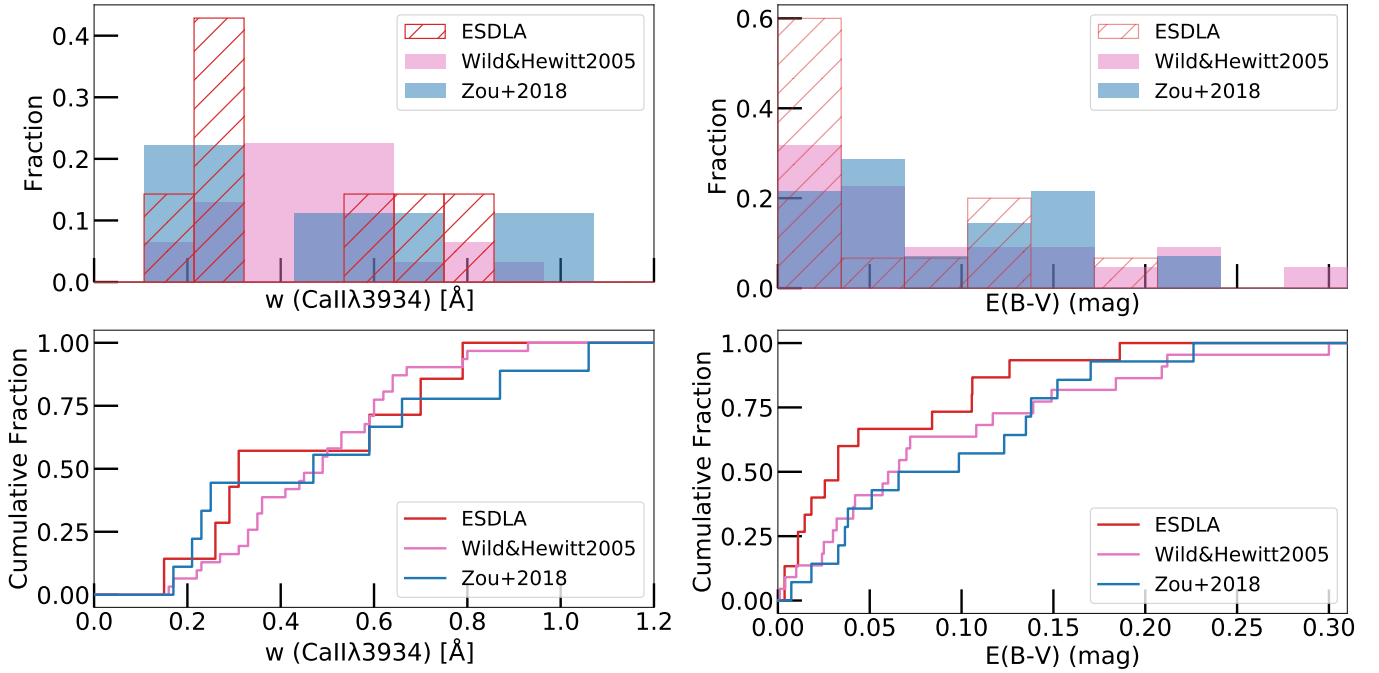


Fig. 4. Distribution of $w(\text{Ca II } \lambda 3934)$ and dust in different samples. *Left panels:* $w(\text{Ca II } \lambda 3934)$ distribution from different samples of DLAs (*top*). ESDLAs are plotted as red lines, while blue and pink shades represent the C I-selected (Zou et al. 2018) and Ca II-selected (Wild & Hewitt 2005) samples, respectively. *Bottom panel:* cumulative distributions for the same samples in the same colours. *Right panels:* similar plot for the measured colour-excess, $E(B - V)$, quantifying dust extinction.

4.7. S II, Ni II, Mn II, Ti II, and P II

In this subsection, we further report the detection of five other singly ionised species, S II, Ni II, Mn II, Ti II, and P II in our sample. These low ionisation species are commonly detected in DLAs. For all five species, the redshift and b -values are tied to other low ionisation species such as Fe II and Si II. We note that Ni II is detected in all ESDLAs, and Mn II is also detected in all ESDLAs, except towards QSO J1513+0352. For this ESDLA, the two Mn II transitions, $\lambda = 1162 \text{ \AA}$ and $\lambda = 1199 \text{ \AA}$, are contaminated by the Ly α forest. The remaining three Mn II transitions, $\lambda = 2576 \text{ \AA}$, $\lambda = 2594 \text{ \AA}$, and $\lambda = 2606 \text{ \AA}$, are strongly blended with the sky residuals in the VIS arm spectra of X-shooter.

Single ionised sulphur (S II) is a good tracer of gas phase metallicity (similar to Zn II) as sulphur is hardly depleted onto dust. However, the relevant S II transitions, $\lambda = 1250 \text{ \AA}$, $\lambda = 1253 \text{ \AA}$, and $\lambda = 1259 \text{ \AA}$, are often contaminated by the Ly α forest lines. Due to this, the robust measurement of the column density is not possible in all cases. For six of our ESDLAs, the S II profiles were free of Ly α contamination. Out of these, the non-blended profile of one system was saturated (towards QSO J0025+1145) and hence we could only estimate the lower limit on $N(\text{S II})$. For another ESDLA system, towards QSO J1258+1212, we found one slightly blended transition, ‘S II $\lambda 1250$ ’, and using that line, we give a tentative estimate on the column density. For the remaining four ESDLAs, towards QSOs J2140–0321, J2232+1242, J2246+1328, and J2322+0033, we obtained a robust estimate on the column density. All the estimations are given in Table A.1.

We further looked for the Ti II transitions at $\lambda = 3384 \text{ \AA}$, $\lambda = 3242 \text{ \AA}$, $\lambda = 3230 \text{ \AA}$, $\lambda = 3073 \text{ \AA}$, $\lambda = 3067 \text{ \AA}$, and $\lambda = 1910 \text{ \AA}$. For all ESDLA rest frames in our study, all mentioned transitions (except $\lambda = 1910 \text{ \AA}$) lie in the NIR arm

region of the X-shooter spectrograph (with the exception of the ESDLA towards QSO J2246+1328 for which the $\lambda = 3073 \text{ \AA}$ and $\lambda = 3067 \text{ \AA}$ transitions also lie in VIS arm region). There is strong contamination from sky lines in the NIR region. In addition, the spectra in the NIR region have significantly lower S/Ns and they are more strongly blended with the sky lines relative to the VIS and UVB band. Using different combinations of the above-mentioned transitions, we obtained a robust estimate of the Ti II column density. For systems where none of the NIR lines can be used for the fit, we report a tentative value for the lower limit using the $\lambda = 1910 \text{ \AA}$ transition. The column density estimates and limits for Ti II are reported in Table A.1.

For most ESDLAs, the P II transitions, $\lambda = 961 \text{ \AA}$, $\lambda = 963 \text{ \AA}$ and $\lambda = 1152 \text{ \AA}$, are strongly contaminated by the Ly α forest and $\lambda = 1301 \text{ \AA}$ and $\lambda = 1532 \text{ \AA}$ are often weak and not detected. We used a combination of multiple transitions mentioned above to obtain a robust column density estimate of P II in ESDLAs towards QSO J1411+1229, J2140–0321, J2232+1242, and J2246+1328. In the appendix, the metal line plots (see Sect. A.2) for all ESDLAs show the relevant transitions used for fitting S II, Ni II, Mn II, Ti II, and P II.

4.8. Dealing with saturation effects for Si II

Absorption lines from Si II are frequently detected in high- z DLAs and they are a good tracer of neutral HI gas. While Si II has a detectable absorption spread over a wide range of rest wavelengths, only a few transitions are outside the Lyman- α forest. For estimating the total column density of Si II, we tied the b -value and redshift of individual Si II, components to Fe II and fitted the observed absorption lines in the spectra with a combination of many Si II transitions with a varying oscillator strength, with namely $\lambda = 989, 1020, 1190, 1193, 1260,$

1304, 1526, 1808, and 2335 Å taking care of possible blending. The total Si II column densities from this analysis are listed in Table 1. However, for some systems, such as ESDLAs toward QSO J0025+1145, J1349+0448, J2140–0321, and J2232+1242, it seems that the absorption profiles of most Si II transitions are saturated. In these cases, in Table 1, we give the allowed range for the Si II column density by getting a conservative upper limit on $N(\text{Si II})$ using the line at $\lambda = 2335$ Å with the weakest oscillator strength.

4.9. Warm and hot gas tracers

In addition to cold gas, a DLA line of sight also reveals ionised warm gas ($T \sim 10^4$ K, traced by Si IV and C IV) and hot gas (traced by N V and O VI), residing in the warm and hot ionised medium as well as the halo of the associated galaxy. Fox et al. (2007) searched for warm and hot gas signatures in DLAs using VLT/UVES data. We searched for the same thing in our medium resolution ESDLA sample.

All the ESDLAs in our sample show absorption lines of warm gas tracers (Si IV and C IV). We performed a multi-component Voigt profile fitting by simultaneously tying the b -value and redshift of all detected warm and hot gas species. Contrary to the plethora of lines for singly ionised species such as Fe II, there are fewer detected lines for warm gas species. Hence, we have to be careful when dealing with intrinsic saturation (see Sect. 4.1 for details). To deal with this issue, we created a mock Voigt absorption profile models for the transitions with a relatively lower oscillator strength – ‘C IV $\lambda 1550$ ’ and ‘Si IV $\lambda 1402$ ’. To create this mock, we needed to estimate a certain minimal b -value for the fitting. The b -value is dependant on the thermal properties of the transition ($b_{\text{thermal}} = \sqrt{2kT/m}$, where k = Boltzmann’s constant, T = temperature of the gas, and m = atomic mass) as well as the turbulence in the medium. Since we do not have any way to distinguish between the two, for a conservative lower limit, we assumed that the gas is non-turbulent and hence, the lower limit on b -value was obtained just from the thermal component. Taking $T \sim 1000$ K, we got b -value ~ 3.7 km s $^{-1}$ for C IV and ~ 2.4 km s $^{-1}$ for Si IV. Using these as lower limit estimates for b -value, we fitted our C IV and Si IV profiles. We note that the b -value for our individual fitted components is always >25 km s $^{-1}$. Assuming that there are no hidden saturated components with a b -value between 2.4 km s $^{-1}$ and 25 km s $^{-1}$, we note that the ‘C IV $\lambda 1550$ ’ and ‘Si IV $\lambda 1402$ ’ profiles have an optical depth, $\tau_0 \sim 1$ at $\log N(\text{C IV}) \sim 14.3$ and $\log N(\text{Si IV}) \sim 13.7$. Any column density measurement higher than these limits might indicate saturation of the line and hence, the corresponding column density estimates are reported as lower limits⁷. Using this information, we report the total column density estimates of C IV and Si IV lines in Table 2. The column density for Si IV and C IV in our sample ranges from 13.3 to >13.7 (in log scale) for Si IV and 13.5 to >14.3 (in log scale) for C IV, respectively. For the ESDLA towards QSO J1349+0448, the Si IV transitions are heavily contaminated by the Ly α forest lines and hence, the corresponding $N(\text{Si IV})$ could not be estimated.

The bottom panel of Fig. 5 shows that the column densities of both of these species, Si IV and C IV, for the general DLA population and ESDLAs are correlated. In the top sub-

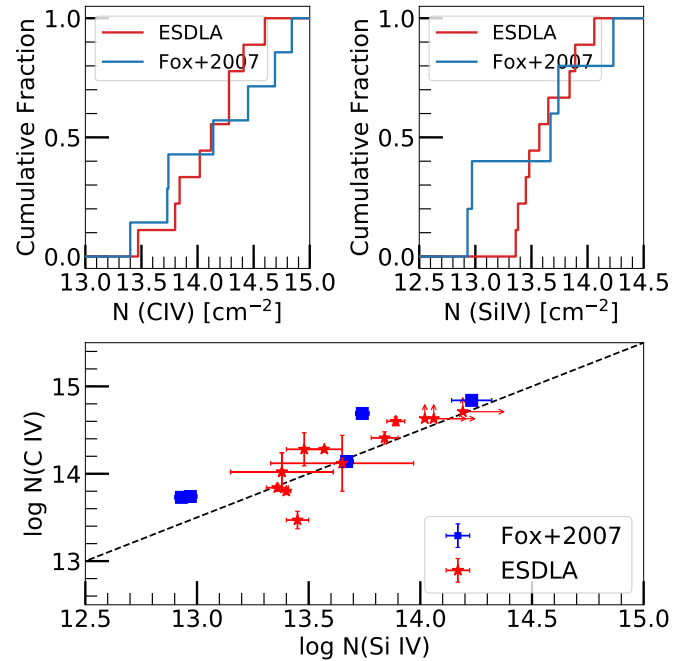


Fig. 5. $N(\text{C IV})$ distribution. *Top left panel:* $\log N(\text{C IV})$ cumulative distributions for the general DLA population (blue line, from Fox et al. 2007) and ESDLAs (red line). *Top right panel:* same for the $\log N(\text{Si IV})$ distributions. *Bottom panel:* $\log N(\text{C IV})$ vs. $\log N(\text{Si IV})$ for ESDLAs (red points) and DLAs (blue points, taken from Fox et al. 2007). The straight line indicates $\log(N(\text{C IV})) = \log(N(\text{Si IV})) + 0.5$.

plots of the figure, we show the cumulative distributions of C IV and Si IV column densities for the general DLA population and ESDLAs. The corresponding high p -values obtained for the K-S tests between the samples [0.74 for $N(\text{C IV})$ and 0.56 for $N(\text{Si IV})$] indicate that they originate from the same distribution. This is expected, as both ESDLA and normal DLA sightlines will also sample warm gas associated with the host galaxy (from their circumgalactic medium, or CGM) despite sampling different H I regions. We note that these warm gas clouds (traced by C IV and Si IV) can also originate from a combined effect of many ionised bubbles present within the interstellar medium (ISM) of the associated galaxy. Yet, this seems unlikely because the cross-section of ionised bubbles in the ISM gas is small (a volume filling factor of ~ 15 – 20% found in studies in the local universe, see Berkhuijsen et al. 2006). There could also be a contribution of warm gas from within the galactic disk originating from a multi-phase ISM model (as described by Ferrière 2001; Cox 2005). More recently, Werk et al. (2019) have shown that the size of the warm ionised medium in the Milky Way can be greater than 1 kpc in size. Given that the typical size of ESDLA galaxies is around ~ 2.5 kpc (see discussions in Guimarães et al. 2012; Ranjan et al. 2018, 2020), we cannot ignore the contribution of warm gas from within the galactic disk. However, it is also imperative from geometry that any sightline passing through the galaxy also has to cross its corresponding CGM. This idea is further supported by the fact that warm gas is detected in all DLAs (including ESDLAs). Hence, the warm gas signature seen in ESDLAs can be from a mixed contribution from both the CGM and the ISM of the associated galaxy.

Due to the Ly α forest confusion, we could not estimate the column density of any hot gas tracer (N V and O VI transitions) in our sample, except towards QSO J1349+0448, in which we detected the ‘N V $\lambda 1238$ ’ transition (fixing the position and

⁷ We note that high spectral resolution ($R \sim 40\,000$) observations would be required to check the presence of any hidden components with a b -value between ~ 2.5 and 25 km s $^{-1}$. We still declare our results as robust assuming that the warm gas b -value would likely have a turbulent component of $b_{\text{turb}} \sim 20$ km s $^{-1}$ or higher.

b -value from C IV). However, we declare this detection as tentative (with $\log N(\text{N V}) \sim 14.16$) as the second transition of the doublet ($\text{N V } \lambda 1242$) is contaminated by the $\text{Ly}\alpha$ forest. We do show the normalised spectra of N V and O VI transitions for some other ESDLA systems (see Appendix A.2), yet they are heavily contaminated with the $\text{Ly}\alpha$ forest lines.

5. Discussion

5.1. Comparing dust-corrected abundances

In absorption line literature, the metallicity of the neutral gas in a system is given as the ratio of the column density of the least dust depleted element, X, to the total hydrogen column density. Volatile elements, such as zinc or sulphur, are commonly used in the literature (see e.g., Kulkarni & Fall 2002), since they are usually accessible in the spectrum and their lines are unsaturated. We note that Zn II was detected in all ESDLAs in our sample and we used Zn (assuming $N(\text{Zn}) = N(\text{Zn II})$ in neutral gas clouds) to calculate the metallicity of ESDLAs in Ranjan et al. (2020)⁸.

Since we obtained the column density of many other neutral gas species in our ESDLA systems, we could further check the dust-corrected metallicity for all ESDLAs. We did this in an attempt to help understand the influence of dust depletion on individual neutral gas tracer species. For this comparison, we corrected the metallicity (say, e.g., $[\text{X}/\text{H}]$, where X = phosphorous, sulphur, silicon, manganese, and chromium) for depletion as per the method described in De Cia et al. (2016) to obtain a depletion-corrected metallicity ($[\text{X}/\text{H}]_c$) for all ESDLA systems with a robust estimate of X (uncertainty in $\log N(\text{X}) < 0.5$). In Fig. 6, we compare the depletion-corrected metallicity obtained using zinc, with metallicities measured based on other singly ionised atomic gas species commonly reported in high- z absorption line studies, such as P II, S II, Si II, Mn II, and Cr II. In the same figure, we also show a straight line indicating $[\text{X}/\text{H}]_c = [\text{Zn}/\text{H}]_c$. We conclude that the dust correction using the method described in De Cia et al. (2016) is robust and that the metallicities calculated using different species are consistent within $\sim 3\sigma$ uncertainty in all cases. We also note that after dust corrections, the metallicity, $[\text{X}/\text{H}]_c$ of ESDLAs range from approximately -1.8 to -0.2 .

5.2. Neutral argon in ESDLAs

The first ionisation potential of argon (15.76 eV) is higher than the H I ionisation threshold (13.6 eV) and hence, argon largely should remain neutral in H I clouds. However, Sofia & Jenkins (1998) showed that the photo-ionisation to recombination rates of Ar I is one order of magnitude higher than H I, indicating that Ar I is quite sensitive to high energy ionising photons. Hence, in the presence of UV-background photons, Ar I might become deficient relative to other α -capture elements, such as silicon and sulphur. Indeed, Jenkins (2013) show that Ar I is deficient in diffuse H I gas in the Milky Way. Zafar et al. (2014) note a similar deficiency in their sample of DLAs observed at high redshift ($2.0 \leq z_{\text{abs}} \leq 4.2$). They conclude that, given the typical DLA metallicity, the deficiency is caused by extragalactic UV photons that ionise neutral argon in the absence of H I self-shielding and

⁸ We note that the uncertainty in $N(\text{Zn II})$ along QSO J2246+1328 was reported incorrectly in Paper I, leading to relatively large errors in metallicity and depletion measurements. The revised value for the Zn II column density along J2246+1328 is $\log N(\text{Zn II}) = 12.52 \pm 0.1$. We further revised the value of metallicity as $[\text{Zn}/\text{H}] = -1.84 \pm 0.1$ and the depletion as $[\text{Fe}/\text{Zn}] = -0.14 \pm 0.13$.

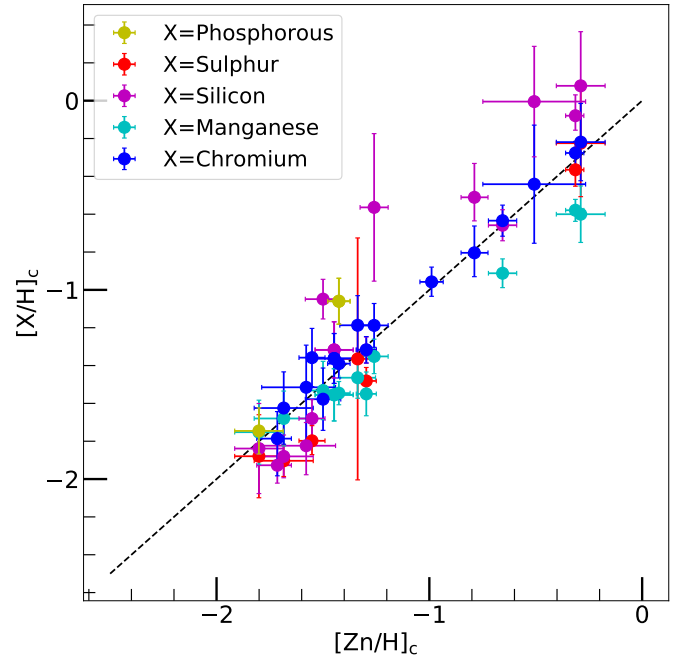


Fig. 6. Depletion-corrected metallicity obtained from different species ($[\text{X}/\text{H}]_c$) as a function of $[\text{Zn}/\text{H}]_c$, where X is a common, singly ionised species found in DLAs as described in the legend. The dashed black line describes $[\text{X}/\text{H}]_c = [\text{Zn}/\text{H}]_c$. The depletion corrections were performed using the equations and information from De Cia et al. (2016).

that such a deficiency should not exist in the presence of high- $N(\text{H I})$ gas clouds originating from within the associated galaxy. Since ESDLAs are high- $N(\text{H I})$ gas clouds with a similar metallicity as DLAs that likely reside within their associated galaxy, our sample is ideal to test this conclusion. Following up on the work of Zafar et al. (2014) (and references therein), we plotted Fig. 7 showing the ratio of Ar I over Si II relative to solar ($[\text{Ar}/\text{Si}]$), as a function of the H I column density.

Zafar et al. (2014) combined modelling with observations to exclude the possibility that Ar I is deficient due to dust depletion or nucleosynthesis and they conclude that the deficiency is due to ionizing photons originating from the extragalactic background at that redshift. Their photo-ionisation models are for gas with solar abundance ratios, low density ($n_{\text{H}} = 0.1 \text{ atoms cm}^{-3}$), and Haardt & Madau (HM) extragalactic background radiation (see Haardt & Madau 2012) at $z = 2.5$. We performed photo-ionisation modelling using the spectral synthesis code CLOUDY (as described by Ferland et al. 2017; Shaw et al. 2005; Shaw & Ferland 2020) using these parameters. We show the models in Fig. 7 as green dots. Zafar et al. (2014) also have a separate set of models with similar parameters and twice the radiation intensity to include the effects of high energy ionising photons. For our analysis, instead of doubling the radiation intensity which would not be physical, we lowered the density of our cloud models (to $n_{\text{H}} = 0.01 \text{ atoms cm}^{-3}$) instead (shown in the figure with purple dots). The lowering of the density is a better assumption also because, if the ESDLAs are made up of multiple gas clouds, we are unsure about the mean particle density in the clouds, even if we know the total column density. We performed additional modelling with an updated background radiation field (from Khaire & Srianand 2019). We assumed a plane parallel gas cloud under constant pressure irradiated from both sides. The gas cloud extends up to a given $N(\text{H I})$. The radiation field consists of cosmic microwave background (CMB)

and Khaire and Srianand (see Khaire & Srianand 2019) meta-galactic radiation at $z = 2.5$ along with diffuse radiation due to in situ star formation. This is similar to the photo-dissociation region (PDR) modelling used to interpret observations of high- z DLAs in the literature (see e.g., Shaw et al. 2016; Rawlins et al. 2018). We used the updated parameters relative to Zafar et al. (2014) to verify that we obtained consistent results. For the new models, we used solar abundance ratios and $\log N(\text{HI})$, ranging from 20 to 22.5. We used a metallicity of $[\text{Zn}/\text{H}] \sim -1.3$ (average ESDLA metallicity) and a density ranging from $n_{\text{H}} = 0.1$ to $n_{\text{H}} = 100 \text{ cm}^{-3}$. Models with $n_{\text{H}} \geq 1$ do not show any under-abundance in the range of $N(\text{HI})$ mentioned. Hence, we do not show these systems in the plot for clarity. We do, however, show the series of models with $n_{\text{H}} = 0.1$ (as cyan dots), which seems to be similar to Zafar et al. (2014) for the high $N(\text{HI})$ regime.

Comparing observations with modelling, we note that for a robust $N(\text{ArI})$ measurement, neutral argon is almost as abundant as singly ionised silicon in ESDLAs and hence, consistent with photoionisation models, there is no pronounced under-abundance of Ar I compared to Si II. Two other ESDLA systems with tentative Ar I detections, towards QSOs J0024–0725 and J1411+1229, show an under-abundance in Ar I (compared to Si II). For these systems, the column density was estimated using only one transition due to strong $\text{Ly}\alpha$ forest blends in the other Ar I transition. Hence, we expect these column density estimates to be quite uncertain. Since, we have no way to robustly quantify the uncertainty (hence the measurements are shown as open stars in the figure), we refrained from interpreting the trend arising from these tentative detections.

Our ESDLA sample result indicates that the argon-silicon column density ratio seems to be increasing as predicted by the photoionisation models at high column densities. The average $[\text{Ar}/\text{Si}]$ in ESDLAs is -0.21 ± 0.1 and that of the photoionisation models is approximately -0.05 for $n_{\text{H}} = 0.1 \text{ cm}^{-3}$ and approximately -0.11 for $n_{\text{H}} = 0.01$ to $n_{\text{H}} = 100 \text{ cm}^{-3}$. We conclude that the mean deficiency of argon as compared to silicon (other α -capture element) as seen by Zafar et al. (2014) in DLAs is non-existent in ESDLAs (within a 2σ uncertainty). There is a residual deficiency of ~ 0.2 dex in the argon-silicon column density ratio in ESDLAs, but as shown by photoionisation models, this can be attributed to low metallicity and/or a number density of the clouds. We conclude that Ar I is likely ionised in low $N(\text{HI})$ (DLAs). This ionisation is likely driven by UV-background photons which cannot penetrate high $N(\text{HI})$ self-shielding ESDLAs. Hence, the under-abundance of Ar I relative to Si II is not seen in ESDLAs.

5.3. Neutral chlorine in H_2 bearing gas

Neutral chlorine (Cl I) is an important tracer of molecular hydrogen as both are connected by charge-exchange reactions. So the production of neutral chlorine (Cl I) is very efficient in the presence of molecular gas (see e.g., Jura 1974). It has been shown in the Milky Way sightlines that there is a direct correlation between $N(\text{H}_2)$ and $N(\text{ClI})$ (see e.g., Jura 1974; Sonnentrucker et al. 2006; Moomey et al. 2012) (see Fig. 8). Using the data points from the literature, Wallström et al. (2019) give a relation between $N(\text{H}_2)$ and $N(\text{ClI})$, holding for up to two orders of magnitude ($18 < \log(N(\text{H}_2)) < 20$), as given below:

$$\log[N(\text{ClI})] = (0.79 \pm 0.06) \times [\log(N(\text{H}_2))] - (2.13 \pm 1.15). \quad (1)$$

This correlation has also been shown to be true for other H_2 bearing high- z DLAs (see e.g., Balashev et al. 2015). The high- z observations available in Balashev et al. (2015)

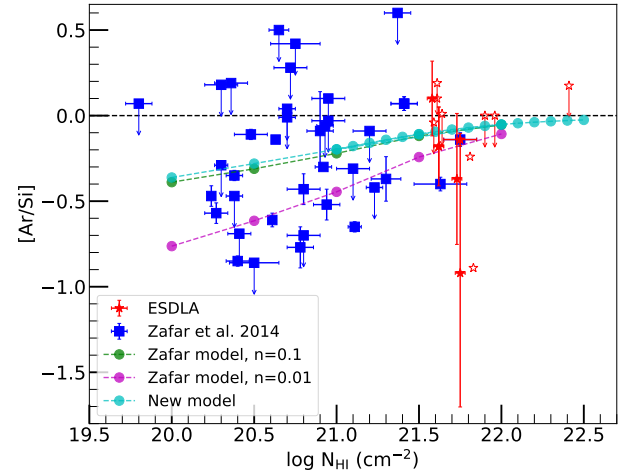


Fig. 7. Ratio of neutral argon Ar I to Si II column density (relative to solar), $[\text{Ar}/\text{Si}]$, plotted as a function of the HI column density. Red stars indicate measurements for ESDLAs from this work, with empty stars indicating tentative detections of Ar I and down arrows representing upper limits. Blue squares are measurements for DLAs from Zafar et al. (2014). The green dots represent a series of photoionisation models run by Zafar et al. (2014) for gas with a solar abundance ratio, low density ($n_{\text{H}} = 0.1 \text{ atoms cm}^{-3}$), and Haardt & Madau (HM) extragalactic background radiation (see Haardt & Madau 2012) at $z = 2.5$. The purple dots also represent similar models, but with a lower density ($n_{\text{H}} = 0.01 \text{ atoms cm}^{-3}$). The cyan points are a series of photo-ionisation models from this work with an updated Khaire & Srianand extragalactic background radiation field (see Khaire & Srianand 2019) and the cosmic microwave background (CMB) at redshift, $z = 2.5$, solar abundance ratios, $\log N(\text{HI})$ ranging from 20 to 22.5, a metallicity of $[\text{Zn}/\text{H}] \sim 0.05$ solar (average ESDLA metallicity), and a density, $n_{\text{H}} = 0.1 \text{ cm}^{-3}$. The photoionisation model results were obtained using CLOUDY.

are limited to $\log N(\text{H}_2) < 20.2$. In our sample, we have an ESDLA system towards QSO J1513+0352 with the highest $\log N(\text{H}_2)$ ($=21.31 \pm 0.01$) amongst QSO-DLAs. Even for such a high $N(\text{H}_2)$, the neutral chlorine measured in this study follows the above-mentioned relation between $N(\text{ClI})$ and $N(\text{H}_2)$. The other two $N(\text{ClI})$ measurements in ESDLAs towards QSO J0025+1145 and J2140–0321 also show consistency with the relation. Further, Noterdaeme et al. (2017) also reported another DLA (towards QSO J0000+0048) with $\log N(\text{H}_2) = 20.43 \pm 0.02$ and $\log N(\text{ClI}) = 14.6 \pm 0.3$. Studies of Cl I-selected metal-rich DLAs (see e.g., Zou et al. 2018; Noterdaeme et al. 2018) report a system towards QSO J0917+0154 with a high $\log N(\text{H}_2) = 20.11 \pm 0.06$ with no significant detection of neutral chlorine (as discussed in a private conversation with the authors of Zou et al. 2018). Balashev et al. (2017) reported an ESDLA towards QSO J0843+0221 with $\log N(\text{H}_2) = 21.21 \pm 0.02$ and $\log N(\text{ClI}) = 13.21 \pm 0.18$. We found that the system, J0843+0221, slightly deviates from the $N(\text{ClI})$ – $N(\text{H}_2)$ relation. The environment of the associated GRB-DLAs (gas probed from the host galaxy associated with a γ -ray burst) have also been shown to be similar to ESDLAs (see Ranjan et al. 2020). In GRB-DLA studies, Heintz et al. (2019) reported a GRB-DLA (towards QSO 181020A) with $\log N(\text{H}_2) = 20.4 \pm 0.04$. We report the neutral chlorine in this GRB-DLA to be $\log N(\text{ClI}) = 14.6 \pm 0.3$ (information received from private conversation with the authors of Heintz et al. 2019). Figure 8 shows all the above discussed data points along with the mentioned $N(\text{ClI})$ – $N(\text{H}_2)$ relation as a straight line. We conclude that the $N(\text{H}_2)$ – $N(\text{ClI})$ relation remains consistent up

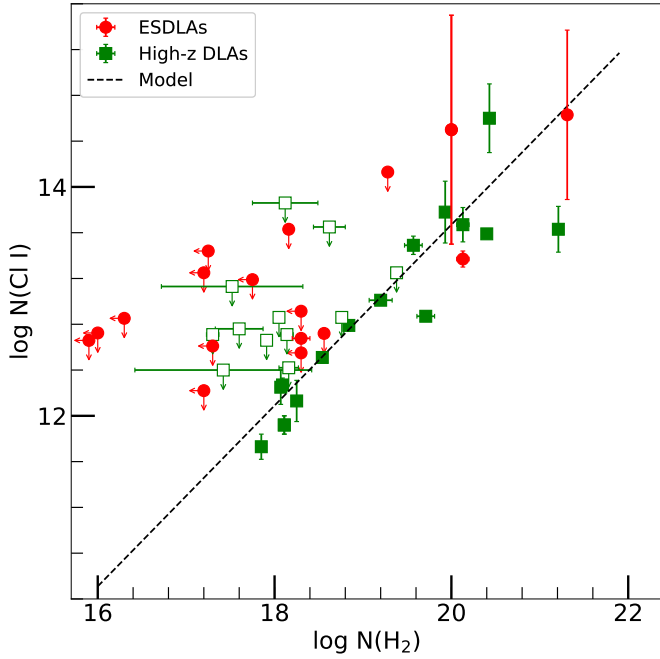


Fig. 8. Neutral chlorine column density ($\log N(\text{Cl I})$) vs. molecular hydrogen column density ($\log N(\text{H}_2)$) in different gas clouds observed in the local universe and high- z as labelled. Most ESDLA points are from this work. Some ESDLA and all high- z DLA points are taken from studies described in the text.

to another two orders of magnitude, $\log(N(\text{H}_2)) < 22$ for all high- z H_2 bearing clouds.

5.4. Mg II in different DLA sub-samples

Strong Mg II absorption ($w(\text{Mg II } \lambda 2796) > 1 \text{ \AA}$) is seen in ESDLAs similar to C I-selected absorbers. Such strong Mg II absorption (high $w(\text{Mg II}) > 1.0 \text{ \AA}$) signatures have been linked with starburst related feedback processes in low mass galactic halos (see Prochter et al. 2006). Although further studies such as Bouché et al. (2012) note that strong Mg II absorption might not always represent strong star-formation activity. Zou et al. (2018) further conjecture that strong Mg II absorption in their sample along with a large velocity spread might be a consequence of either an interaction or star-formation activity in the associated galaxy. To continue this discussion further, we compared the $N(\text{H I})$, metallicity, velocity spread, $\Delta v(\text{Mg II } \lambda 2796)$, and equivalent width, $w(\text{Mg II } \lambda 2796)$, for Mg II-selected DLAs from Matejek et al. (2013), C I-selected absorbers from Zou et al. (2018), and ESDLAs from this work. We attempted to understand different properties of these sub-samples that are shown to be associated with galaxies by comparing their corresponding Mg II profiles.

To explore these, Fig. 9 shows the plots between $N(\text{H I})$, metallicity ($\log Z$), $\Delta v(\text{Mg II } \lambda 2796)$, and $w(\text{Mg II } \lambda 2796)$. We found that ESDLA metallicity strongly correlates with $\Delta v(\text{Mg II } \lambda 2796)$, Pearson correlation coefficient, $r = 0.79$ and $w(\text{Mg II } \lambda 2796)$, $r = 0.91$. We also see a correlation between $N(\text{H I})$ of C I-selected DLAs and $\Delta v(\text{Mg II } \lambda 2796)$, $r = 0.58$. We note that while both C I-selected absorbers and ESDLAs have a high Mg II equivalent width (compared with general DLAs), the associated kinematics of Mg II indicate that these two sets may be sampling different populations of galaxies.

We note that while C I-selected DLAs were targeted to have a high C I content and were found to have a high metallicity and ESDLAs to be of high $N(\text{H I})$ by definition, they do indeed probe low $N(\text{H I})$ and low metallicity gas consecutively. Although, the absence of metal-rich high $N(\text{H I})$ gas might just represent the limitation of our selection criteria. Metal- and dust-rich systems will be missed in the optical colour-excess selection based criteria (see Richards et al. 2002) for observing QSOs as used by SDSS. Future surveys such as DESI that implement a more robust selection combining optical and NIR colours (see Yèche et al. 2020) might help understand whether such systems were just missed in our observations or are indeed rarer to find.

In kinematics-metallicity space, we show that ESDLAs and C I-selected absorbers are clearly distinct entities, while their $w(\text{Mg II } \lambda 2796)$ distribution is similar. The C I-selected sample shows high kinematical extension (measured as a Δv value for their ‘Mg II $\lambda 2796$ ’ absorption profile) with all but four (out of 17) systems having ‘Mg II $\lambda 2796$ ’ $\Delta v > 300 \text{ km s}^{-1}$. Figure 10 plots the Δv against the equivalent width (w) of ‘Mg II $\lambda 2796$ ’ line. We can see that in comparison to C I-selected absorbers, ESDLAs have a relatively lower kinematical extension (only six out of 18 systems have $\Delta v > 300 \text{ km s}^{-1}$). In addition to having a high Δv value, Zou et al. (2018) also show that some of their DLAs have subsystems in which the Mg II and C I absorption profiles are separated by more than $\sim 200 \text{ km s}^{-1}$, termed as gas with disturbed kinematics in their work. In this work, Mg II and C I profiles (see Ranjan et al. 2018, 2020) in ESDLAs do not show such disturbed kinematics as opposed to what is seen in C I-selected clouds. This is representative of different origins for the ESDLA gas clouds compared to C I-selected absorbers.

As discussed in literature, the connection of strong Mg II absorbers ($w(\text{Mg II } \lambda 2796) > 1 \text{ \AA}$) with star-formation activity is rather ambiguous. In addition, the current observations using X-shooter and other high-resolution ground-based spectrographs do not detect the galaxy stellar continuum in any of the samples discussed above. While emission lines have been detected in ESDLAs that indicate a modest instantaneous star-formation rate (see Ranjan et al. 2020), they are not enough to form a general consensus about the galaxy morphology. Rafelski et al. (2016) note that the star-formation rate (SFR) deficiency in DLAs are a consequence of poor conversion efficiency of H I to H_2 in low metallicity environments. While we do note that ESDLAs are metal-poor compared to C I-selected absorbers, the presence of H_2 is high in ESDLAs (more than half of the ESDLAs have confirmed diffuse H_2 detection), similar to the C I-selected sample. Although, ESDLAs are dust-poor ($A_V \sim 0.1$) and due to our limited line of sight study, there is no way to confirm as to how much of this diffuse H_2 gas indeed cools down to form fully molecular regions that can further form stars. Using the analysis above, we conclude that, while C I-selected absorbers and ESDLAs indeed probe different environments, no strong conclusion can be drawn by this about the nature of star formation in their associated galaxy.

5.5. Trend of Ca II with dust

The presence of calcium (as Ca II) in high- z DLAs and sub-DLAs have been linked to dusty gas systems from within the halo of their associated galaxy. Calcium gets depleted onto dust

⁹ We note that the Δv mentioned here is measured for saturated or intrinsically saturated lines for both C I-selected absorbers and ESDLAs and hence cannot be compared with the standard Δv_{90} measurements of unsaturated lines (as shown in Ledoux et al. 2006).

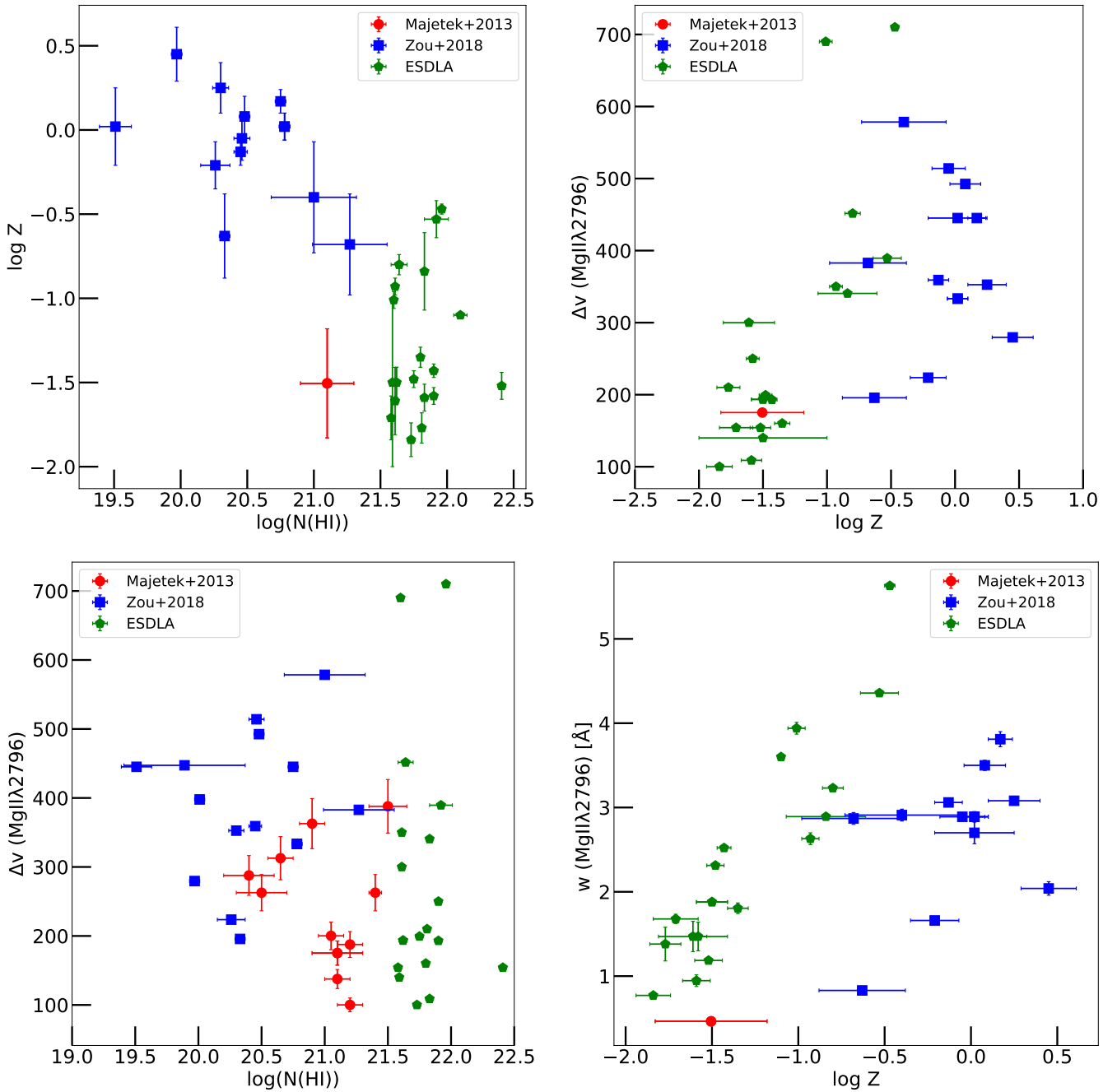


Fig. 9. Comparison between properties of Mg II profiles in different samples. *Top left panel:* $\log N(\text{H I})$ [atoms cm^{-2}] vs. metallicity ($\log Z = [X/\text{H}]$). *Top right panel:* $\Delta v(\text{Mg II } \lambda 2796)$ [km s^{-1}] vs. metallicity ($\log Z$). *Bottom left panel:* equivalent width $w(\text{Mg II } \lambda 2796)$ [\AA] vs. $\log N(\text{H I})$ [atoms cm^{-2}]. *Bottom right panel:* equivalent width $w(\text{Mg II } \lambda 2796)$ [\AA] vs. metallicity ($\log Z$) for ESDLAs (green pentagons, this work), C I-selected absorbers (blue points, from Zou et al. 2018), and the Mg II-selected DLAs (red circles, from Matejek et al. 2013).

and hence, the Ca II column density does not necessarily scale linearly with dust. The ionisation potential of Ca II is 11.87 eV and is lower than H I (13.6 eV) and hence, Ca II is not the main ionisation state of calcium in H I gas. Nestor et al. (2008) indicated that the systems with $w(\text{Ca II}) > 0.25 \text{ \AA}$ should be DLAs. We note that, among robust detections, all our ESDLAs fulfil this criterion except the ESDLA towards QSO J1513+0352. We note that this is the only ESDLA in our sample with Ly α emission detected in proximity as well as the presence of higher rotational levels of H₂ (see Ranjan et al. 2018), indicating a possibly enhanced radiation environment as compared to other ESDLAs.

Such enhanced radiation might ionise Ca II significantly to show the observed under-abundance. However, further investigation of the effects of radiation on Ca II requires detailed modelling and is beyond the scope of discussion for this article.

Studies in the literature (such as Zych et al. 2009) also suggest that absorbers with $w(\text{Ca II } \lambda 3934) \gtrsim 0.7 \text{ \AA}$ should probe diffuse H₂ gas clouds from within their associated galactic disks. However, Ca II is easily depleted onto dust and hence, it does not simply correlate with $N(\text{H}_2)$ in diffuse gas clouds with a moderate dust content ($0.2 < A_V < 1$). The ESDLAs toward QSOs J0025+1145, J1411+1229, and J2359+1354 fulfil this

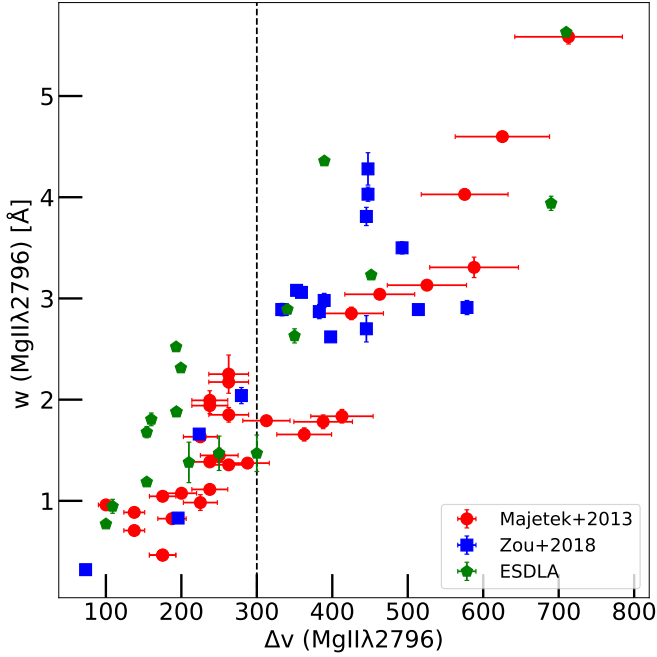


Fig. 10. Velocity spread Δv vs. the equivalent width (w) of the ‘Mg II $\lambda 2796$ ’ absorption line for C I-selected absorbers (taken from Zou et al. 2018), Mg II-selected DLAs (taken from Majecek et al. 2013), and ESDLAs (from this work). The dashed black vertical line represents $\Delta v(\text{Mg II } \lambda 2796) = 300 \text{ km s}^{-1}$.

criterion. We found traces of H_2 in ESDLAs towards QSO J0025+1145 (with $A_V = 0.51$) in Ranjan et al. (2020) and J2359+1354 (with $A_V = 0.29$) (Telikova et al. 2022). In J0025+1145, we also found ‘[O III] $\lambda 5007$ ’ and $\text{H-}\alpha$ emission in very close proximity ($\rho = 1.9 \pm 0.1 \text{ kpc}$) to the absorber line of sight, indicating that the gas originates from within the star-forming disk of the associated galaxy. However, we did not find a significant trace of H_2 in the ESDLA system towards QSO J1411+1229. Since the survival of H_2 is associated with dust, the extremely low dust content ($A_V = 0.09$) as compared to the other two cases can be the reason for the absence of H_2 .

In the local universe, Nestor et al. (2008) initially showed that $w(\text{Ca II } \lambda 3934)$ might not increase linearly with $N(\text{HI})$. However, later studies from the local universe (such as Murga et al. 2015, and references therein) indicate an increasing trend of $N(\text{HI})$ and $E(B - V)$ with increasing $w(\text{Ca II } \lambda 3934)$. Yet the trend disappears once saturation effects become significant (at $N(\text{HI}) \sim 5 \times 10^{20} \text{ cm}^{-2}$ and $E(B - V) \sim 0.08 \text{ mag}$). At high- z , Wild & Hewett (2005) were the first to search the SDSS catalogue for Ca II-bearing absorbers and they reported a trend of increasing dust content with an equivalent width of Ca II. Although they also mention that $\sim 40\%$ of the Ca II absorbers would be missed due to the optical selection criteria of SDSS. Nestor et al. (2008) further noted that no trend was found between the Ca II equivalent width and metallicity or degree of depletion. They also noted that the strength of Ca II lines is determined by a combination of particle density, background UV photons, and the dust content of the gas clouds. Zou et al. (2018) also state that the relation between $w(\text{Ca II } \lambda 3934)$ and dust reddening $E(B - V)$ is ambiguous for high- z observations.

Given that our ESDLAs sample metal- and dust-poor environments that are, as of yet, often H_2 bearing (at least for 50% of the cases), we intend to check whether we see any similar trend as mentioned above. Figure 11 shows the plot

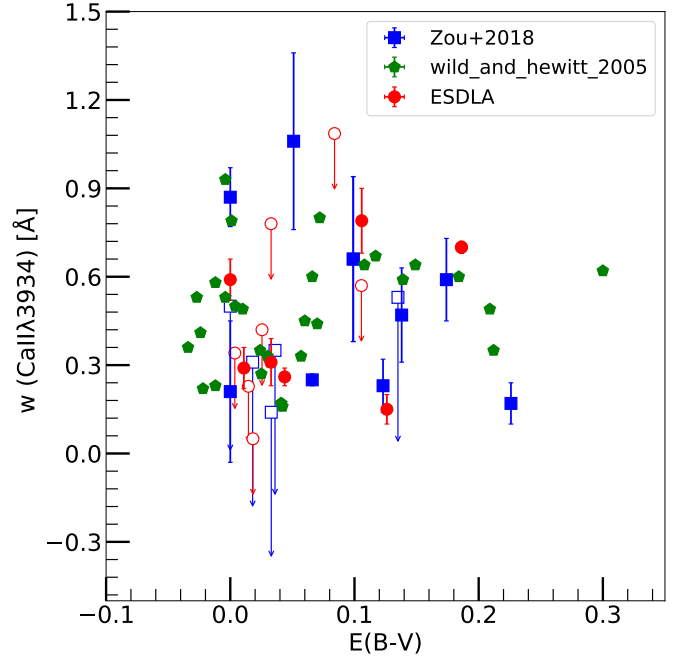


Fig. 11. Equivalent width, $w(\text{Ca II } \lambda 3934)$, as a function of the colour excess $E(B - V)$. The red circles, blue squares, and green pentagons represent the ESDLAs, as well as the C I-selected (Zou et al. 2018) and Ca II-selected (Wild & Hewett 2005) sample, respectively. The $w(\text{Ca II } \lambda 3934)$ upper limits are represented by a hollow shape and a down arrow.

of $w(\text{Ca II } \lambda 3934)$ versus $E(B - V)$ for ESDLAs in our sample, the C I-selected absorbers from Zou et al. (2018), and the Ca II-selected sample from Wild & Hewett (2005). The figure shows that $w(\text{Ca II } \lambda 3934)$ does not correlate with $E(B - V)$ globally or even in the individual high- z samples. Hence, we cannot conclude that there is any strong trend of $w(\text{Ca II } \lambda 3934)$ with dust extinction in high- z absorbers. We note that this lack of a trend cannot be necessarily attributed to a low dust content ($E(B - V) \lesssim 0.3$) in QSO absorber samples. The correlation between $w(\text{Ca II } \lambda 3934)$ and $E(B - V)$ is seen in previous studies for samples with $E(B - V) < 0.08$ and $w(\text{Ca II } \lambda 3934) < 0.35$. However, for all high- z absorbers seen here, there seems to be no significant correlation between $w(\text{Ca II } \lambda 3934)$ and $E(B - V)$. We also checked for correlation in sub-samples with $E(B - V) < 0.08$ and $w(\text{Ca II } \lambda 3934) < 0.35$ and found no significant correlation to report. Probing dustier sightlines ($E(B - V) \gtrsim 0.3$), which might be possible in future deeper surveys such as DESI (see Yèche et al. 2020) and WEAVE-QSO (see Pieri et al. 2016), will help understand if there is any strong trend of $w(\text{Ca II } \lambda 3934)$ with dust in absorbers with ($E(B - V) \gtrsim 0.3$).

5.6. Kinematics

ESDLAs provide a unique opportunity to study the nature of gas, not only from within the star-forming disk of an associated faint galaxy (see Ranjan et al. 2020), but also study the warm and hot medium associated with it. Since ESDLAs do probe gas from within the galactic disk, they are likely to probe warm and hot gas both from within the disk (see discussion in Sect. 4.9) and the outskirts of the associated galaxy. Warm gas is likely to have relatively disturbed kinematics as compared to their neutral gas counterparts. Fox et al. (2007) showed that the mean $\Delta v_{90}(\text{C IV})$ is approximately twice that of the mean

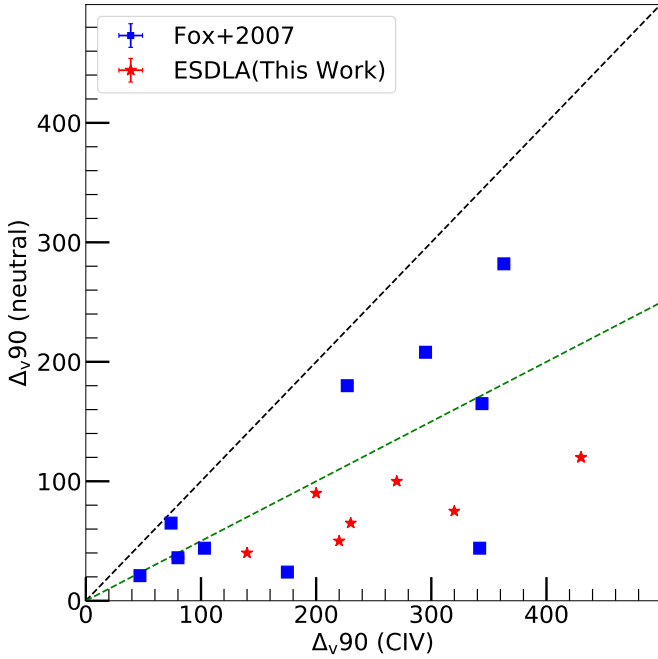


Fig. 12. Comparison between Δv_{90} estimates of warm gas (C IV) (from this work) and neutral gas as obtained from unsaturated transitions of singly ionised species such as Zn II and Fe II in different ESDLAs (taken from [Ranjan et al. 2020](#)) and DLAs (taken from [Fox et al. 2007](#)). The dashed black and green lines indicate $\Delta v_{90}(\text{C IV}) = \Delta v_{90}(\text{neutral})$ and $\Delta v_{90}(\text{C IV}) = 2 \times \Delta v_{90}(\text{neutral})$, respectively.

$\Delta v_{90}(\text{neutral})$. In our ESDLA sample, we make a similar comparison of the standard Δv_{90} measurements of singly ionised unsaturated lines (taken from [Ranjan et al. 2020](#)) and shown in Table 1) with the Δv_{90} of unsaturated C IV profiles. We see that the mean $\Delta v_{90}(\text{C IV}) (= 260 \text{ km s}^{-1})$ is ~ 3 times the mean $\Delta v_{90}(\text{neutral}) (= 80 \text{ km s}^{-1})$ for unsaturated lines indicating less disturbed HI gas in ESDLAs compared to DLAs. Figure 12 shows the distribution of kinematics (Δv_{90}) of unsaturated C IV and neutral gas. We show that the distribution has a large spread, but the Δv_{90} of C IV gas is larger than neutral gas for all the absorbers. We also note that this is especially evident for ESDLAs as the neutral gas is much less disturbed. While the distribution of Δv_{90} of C IV gas is quite similar for DLAs and ESDLAs (as evident in Figs. 5 and 12), the Δv_{90} of neutral gas in ESDLAs is smaller than that of DLAs. Figure 12 further shows that the Δv_{90} of C IV profiles is always more than double than that of Δv_{90} of neutral gas in ESDLAs, while the same is not true for DLAs. In DLAs, the Δv_{90} of neutral gas can be higher in many cases. In addition, the average metallicity of the DLAs of [Fox et al. 2007](#) is -1.68 ± 0.08 , which is also lower than that of the ESDLAs (-1.30 ± 0.05). Hence, this trend in Δv_{90} of neutral gas cannot be attributed to the standard Δv_{90} -metallicity relation. Using the above argument, we conclude that while the Δv_{90} of C IV in DLAs and ESDLAs are not distinguishable, HI gas is statistically less disturbed for ESDLAs (with a relatively smaller Δv_{90}) and hence, indicative of different origins of the HI gas in DLAs and ESDLAs.

6. Summary

We study a sample of extremely strong damped Ly α absorber systems (ESDLAs) observed in medium and higher spectral resolution spectra towards quasars. In [Ranjan et al. \(2020\)](#), we

reported the column density and kinematics of HI gas, diffuse H₂ and some associated species in addition to reporting the emission signatures from nearby star-forming regions. The impact parameter of these absorbers relative to the centroid of the emission indicates that ESDLAs originate from the star-forming disk of their associated galaxies. In this paper, we extend our analysis towards the multi-phase nature of ESDLAs. We measured the column density and equivalent width and kinematics (Δv_{90}) of low ionisation species (such as O I, Ar I, C II, N I, Na I, Mg II, Ca II, S II, Ni II, Mn II, Ti II, and P II). We found tracers of all of these species in different systems, except for Na I. We also looked for signatures of warm and hot gas tracers (C IV, Si IV, N V, and O VI) associated with these ESDLAs and identified all these species in different ESDLAs, except for O VI. Since O VI transitions are heavily contaminated with Ly α forest, it was difficult to confirm their detection. Although, the presence of O VI in ESDLAs cannot be ruled out.

We further compare the distribution of column densities, equivalent widths, and kinematics of the above-mentioned species with other absorber samples, which are known to probe gas associated with galaxies. Specifically, we compare our ESDLAs with the Mg II-selected DLA population (studied by [Matejek et al. 2013](#)), dusty gas clouds probed using Ca II H-K absorption bands (studied by [Wild & Hewett 2005](#)), metal-rich C I-selected absorbers (studied by [Zou et al. 2018](#)), and C IV absorption (studied in the DLA sample by [Fox et al. 2007](#)). ESDLAs and DLAs have the same column density distribution for their warm gas tracers, C IV and Si IV. The robust estimate of N V and O VI column densities are not possible in our medium resolution study due to the contamination by Ly α forest absorption lines.

We estimate dust-corrected metallicity measured using different neutral gas species such as P II, S II, Si II, Mn II, and Cr II and compare it with the standard Zn II-based measurements, which is common in DLA literature. We find that, after applying dust correction as prescribed by [De Cia et al. \(2016\)](#), the measured metallicities are consistent for all mentioned species in all ESDLAs within a 3σ uncertainty.

By comparing the neutral argon (Ar I) in ESDLAs and DLAs, we conclude that the distribution of [Ar/H] in DLAs is similar to our sample of ESDLAs. We also note that the under-abundance of Ar I compared to α -elements as found in DLAs (see [Zafar et al. 2014](#)) do not extend to our ESDLA subsample. [Zafar et al. \(2014\)](#) claim that as opposed to dust depletion, or nucleosynthesis effects, the mentioned under-abundance is caused by background UV photons ionising the Ar I in DLAs. They also conclude that, in the presence of self-shielding high $N(\text{HI})$ gas, Ar I should be able to survive. As our sample has high $N(\text{HI})$, we tested this hypothesis. Comparing our observations and with updated CLOUDY photo-ionisation models, we conclude that ESDLAs do not show any under-abundance of Ar I relative to another α -capture element, silicon relative to the photoionisation models. Hence, the ionisation seen in DLAs is likely driven by UV-background photons that cannot penetrate the high $N(\text{HI})$ in ESDLAs. We further note that a residual under-abundance of Ar I relative to Si II of ~ 0.2 dex in ESDLAs can be attributed to the low metallicity of ESDLAs.

Compared to the Mg II-selected DLA population, we detect a large equivalent width, $w(\text{Mg II } \lambda 2796)$, for some ESDLAs similar to some metal-rich C I-selected absorbers. Although, we note that ESDLAs and C I-selected samples can have a rather different velocity spread (Δv) of ‘Mg II $\lambda 2796$ ’. In the combined sample of Mg II-selected DLAs, ESDLAs, and C I-selected absorbers,

we find a correlation between metallicity and velocity spread. The dust extinction, $E(B - V)$, and $w(\text{Ca II}\lambda 3934)$ distribution in ESDLAs is quite similar to that of C I- and Ca II-selected absorbers.

We study the relationship between $N(\text{H}_2)$ and $N(\text{C I I})$, previously studied in the literature (see e.g., Balashev et al. 2015). By extending studies in literature (with ESDLAs and other translucent clouds with $\log(N(\text{H}_2)) > 20$), we note that the $N(\text{C I I})-N(\text{H}_2)$ correlation shown in the literature is consistent even for high $N(\text{H}_2)$ translucent clouds (up to $\log N(\text{H}_2) < 22$). We conclude that the H_2 production seems as favourable in gas clouds with a low metallicity and high $N(\text{H I})$ environments (such as ESDLAs) as they are in metal-rich, relatively lower $N(\text{H I})$ environments (such as C I-selected systems studied by Zou et al. 2018, and reference therein). Additionally, we report a strong Ca II presence ($w(\text{Ca II}) > 0.3 \text{ \AA}$) in most of our ESDLAs. By comparing the dust extinction measurement with the Ca II measurement, we also conclude that $w(\text{Ca II}\lambda 3934)$ does not correlate with the dust content in different high- z absorbers. Although, the dust content in all absorbers discussed above is rather limited ($E(B - V) \leq 0.3$). We note that this might be indicative of the SDSS optical colour-excess selection technique (see Richards et al. 2002) being biased towards dust-poor absorbers. Future large-sky surveys such as DESI that use a more robust selection technique combining optical colour with NIR band colour from the Wide-field Infrared Survey Explorer (WISE) (see e.g., Yèche et al. 2020) will likely probe dustier ($A_V \sim 1$), possibly metal-rich, high $N(\text{H}_2)$ gas environments towards QSOs. These samples could be then used for robust comparison between high $N(\text{H}_2)$ metal-rich systems and ESDLAs.

The column density and kinematics of C IV and Si IV associated with ESDLAs are similar to those found in DLAs. This is expected as both DLA and ESDLA sightlines will sample warm gas in the CGM and the warm neutral medium associated with their host galaxy despite sampling different H I regions. Interestingly, the Δv_{90} of a warm ionised medium (traced by unsaturated C IV lines) is always more than double that of H I gas (traced by an unsaturated, singly ionised species such as Fe II and Zn II) in ESDLAs. This trend is not often seen in DLAs. We also show that the Δv_{90} of the H I region in DLAs are higher than in ESDLAs, despite having a lower average metallicity as compared to ESDLAs. This indicates that the H I regions sampled by DLAs might be different to the H I regions sampled by ESDLAs.

ESDLAs provide a unique way to study gas within a metal-poor, general galaxy population at a high redshift and hence, warrant follow-up studies of their physical properties and kinematics. We believe that future studies of ESDLAs in higher spectral resolution ($R \sim 40\,000$) will help model the physical conditions for each individual ESDLA. In addition, the NIR-optical-based QSO selection technique in large sky surveys such as WEAVE-QSO and DESI will help identify if dustier ($A_V \sim 1$) ESDLA environments also exist.

Acknowledgements. P.P.J. thanks allegorical Camille Noûs (Laboratoire Cogitamus) for inappreciable and often unnoticed discussions, advice and support. G.S. acknowledges WOS-A grant from Department of Science and Technology (SR/WOS-A/PM-9/2017). Y.K.S. and A.R. acknowledge support from the National Research Foundation of Korea (NRF) grant funded by the Ministry of Science and ICT (NRF-2019R1C1C1010279). S.B. and K.T. are supported by RSF grant 18-12-00301. We thank the authors of Telikova et al. (2020, 2022), Zou et al. (2018), and Heintz et al. (2019) for providing us useful information about their sample. We thank Pasquier Noterdaeme and J.-K. Krogager for help with the observations and comments on early versions of the manuscript.

References

- Abgrall, H., & Roueff, E. 2006, *A&A*, 445, 361
- Altay, G., Theuns, T., Schaye, J., Booth, C. M., & Dalla Vecchia, C. 2013, *MNRAS*, 436, 2689
- Baillya, D., Salumbidesby, E., Vervloet, M., & Ubachs, W. 2010, *Mol. Phys.*, 108, 827
- Balashev, S. A., & Noterdaeme, P. 2018, *MNRAS*, 478, L7
- Balashev, S. A., Noterdaeme, P., Klimenko, V. V., et al. 2015, *A&A*, 575, L8
- Balashev, S. A., Noterdaeme, P., Rahmani, H., et al. 2017, *MNRAS*, 470, 2890
- Berengut, J. C., Dzuba, V. A., Flambaum, V. V., et al. 2011, *Astrophys. Space Sci. Proc.*, 22, 9
- Bergeron, J., & Boissé, P. 1991, *A&A*, 243, 344
- Berkhuijsen, E. M., Mitra, D., & Mueller, P. 2006, *Astron. Nachr.*, 327, 82
- Bouché, N., Murphy, M. T., & Péroux, C. 2004, *MNRAS*, 354, L25
- Bouché, N., Murphy, M. T., Péroux, C., Csabai, I., & Wild, V. 2007, *New Astron. Rev.*, 51, 131
- Bouché, N., Murphy, M. T., Péroux, C., et al. 2012, *MNRAS*, 419, 2
- Carswell, R. F., & Webb, J. K. 2014, *Astrophysics Source Code Library* [record:1408.015]
- Cox, D. P. 2005, *ARA&A*, 43, 337
- Crawford, I. A. 1992, *MNRAS*, 259, 47
- Crighton, N. H. M., Murphy, M. T., Prochaska, J. X., et al. 2015, *MNRAS*, 452, 217
- De Cia, A., Ledoux, C., Mattsson, L., et al. 2016, *A&A*, 596, A97
- Feltre, A., Bacon, R., Tresse, L., et al. 2018, *A&A*, 617, A62
- Ferland, G. J., Chatzikos, M., Guzmán, F., et al. 2017, *Rev. Mex. Astron. Astrofis.*, 53, 385
- Ferrière, K. M. 2001, *Rev. Mod. Phys.*, 73, 1031
- Fox, A. J., Ledoux, C., Petitjean, P., & Srianand, R. 2007, *A&A*, 473, 791
- Fox, A. J., Ledoux, C., Vreeswijk, P. M., Smette, A., & Jaunsen, A. O. 2008, *A&A*, 491, 189
- Fynbo, J. P. U., Krogager, J.-K., Venemans, B., et al. 2013, *ApJS*, 204, 6
- Guimarães, R., Noterdaeme, P., Petitjean, P., et al. 2012, *AJ*, 143, 147
- Haardt, F., & Madau, P. 2012, *ApJ*, 746, 125
- Heintz, K. E., Bolmer, J., Ledoux, C., et al. 2019, *A&A*, 629, A131
- Ivanov, T. I., Salumbides, E. J., Vieitez, M. O., et al. 2008, *MNRAS*, 389, L4
- Jenkins, E. B. 2013, *ApJ*, 764, 25
- Jura, M. 1974, *ApJ*, 191, 375
- Khaire, V., & Srianand, R. 2019, *MNRAS*, 484, 4174
- Krogager, J.-K., Møller, P., Fynbo, J. P. U., & Noterdaeme, P. 2017, *MNRAS*, 469, 2959
- Kulkarni, V. P., & Fall, S. M. 2002, *ApJ*, 580, 732
- Kulkarni, V. P., Som, D., Morrison, S., et al. 2015, *ApJ*, 815, 24
- Ledoux, C., Petitjean, P., & Srianand, R. 2003, *MNRAS*, 346, 209
- Ledoux, C., Petitjean, P., Fynbo, J. P. U., Møller, P., & Srianand, R. 2006, *A&A*, 457, 71
- Ledoux, C., Noterdaeme, P., Petitjean, P., & Srianand, R. 2015, *A&A*, 580, A8
- Matejek, M. S., Simcoe, R. A., Cooksey, K. L., & Seyffert, E. N. 2013, *ApJ*, 764, 9
- Meynet, G., & Maeder, A. 2002, *A&A*, 390, 561
- Modigliani, A., Goldoni, P., Royer, F., et al. 2010, *Proc. SPIE*, 7737, 773728
- Mooney, D., Ferman, S. R., & Sheffer, Y. 2012, *ApJ*, 744, 174
- Morton, D. C. 2003, *ApJS*, 149, 205
- Murga, M., Zhu, G., Ménard, B., & Lan, T.-W. 2015, *MNRAS*, 452, 511
- Nestor, D. B., Pettini, M., Hewett, P. C., Rao, S., & Wild, V. 2008, *MNRAS*, 390, 1670
- Noterdaeme, P., Ledoux, C., Petitjean, P., et al. 2007, *A&A*, 474, 393
- Noterdaeme, P., Ledoux, C., Petitjean, P., & Srianand, R. 2008, *A&A*, 481, 327
- Noterdaeme, P., Petitjean, P., Ledoux, C., & Srianand, R. 2009, *A&A*, 505, 1087
- Noterdaeme, P., Petitjean, P., Carithers, W. C., et al. 2012a, *A&A*, 547, L1
- Noterdaeme, P., Laursen, P., Petitjean, P., et al. 2012b, *A&A*, 540, A63
- Noterdaeme, P., Petitjean, P., Pâris, I., et al. 2014, *A&A*, 566, A24
- Noterdaeme, P., Petitjean, P., & Srianand, R. 2015a, *A&A*, 578, L5
- Noterdaeme, P., Srianand, R., Rahmani, H., et al. 2015b, *A&A*, 577, A24
- Noterdaeme, P., Krogager, J.-K., Balashev, S., et al. 2017, *A&A*, 597, A82
- Noterdaeme, P., Ledoux, C., Zou, S., et al. 2018, *A&A*, 612, A58
- Oliveira, C. M., & Hébrard, G. 2006, *ApJ*, 653, 345
- Péroux, C., Bouché, N., Kulkarni, V. P., York, D. G., & Vladilo, G. 2012, *MNRAS*, 419, 3060
- Péroux, C., Rahmani, H., Arrigoni Battaia, F., & Augustin, R. 2018, *MNRAS*, 479, L50
- Petitjean, P., & Aracil, B. 2004, *A&A*, 422, 523
- Petitjean, P., Srianand, R., & Ledoux, C. 2000, *A&A*, 364, L26
- Petitjean, P., Ledoux, C., & Srianand, R. 2008, *A&A*, 480, 349
- Pieri, M. M., Bonoli, S., Chaves-Montero, J., et al. 2016, in SF2A-2016: *Proceedings of the Annual meeting of the French Society of Astronomy and Astrophysics*, eds. C. Reylé, J. Richard, L. Cambrésy, et al., 259

- Pontzen, A., Governato, F., Pettini, M., et al. 2008, *MNRAS*, 390, 1349
- Prochaska, J. X., Herbert-Fort, S., & Wolfe, A. M. 2005, *ApJ*, 635, 123
- Prochter, G. E., Prochaska, J. X., Chen, H.-W., et al. 2006, *ApJ*, 648, L93
- Rafelski, M., Gardner, J. P., Fumagalli, M., et al. 2016, *ApJ*, 825, 87
- Rahmani, H., Péroux, C., Turnshek, D. A., et al. 2016, *MNRAS*, 463, 980
- Rahmati, A., & Schaye, J. 2014, *MNRAS*, 438, 529
- Ranjan, A., Noterdaeme, P., Krogager, J.-K., et al. 2018, *A&A*, 618, A184
- Ranjan, A., Noterdaeme, P., Krogager, J. K., et al. 2020, *A&A*, 633, A125
- Rao, S. M., Prochaska, J. X., Howk, J. C., & Wolfe, A. M. 2005, *AJ*, 129, 9
- Rawlins, K., Srianand, R., Shaw, G., et al. 2018, *MNRAS*, 481, 2083
- Richards, G. T., Fan, X., Newberg, H. J., et al. 2002, *AJ*, 123, 2945
- Salumbides, E. J., Hannemann, S., Eikema, K. S. E., & Ubachs, W. 2006, *MNRAS*, 373, L41
- Sánchez-Ramírez, R., Ellison, S. L., Prochaska, J. X., et al. 2016, *MNRAS*, 456, 4488
- Schechtman, R. M., Federman, S. R., Beideck, D. J., & Ellis, D. J. 1993, *ApJ*, 406, 735
- Shaw, G., & Ferland, G. J. 2020, *MNRAS*, 493, 5153
- Shaw, G., Ferland, G. J., Abel, N. P., Stancil, P. C., & van Hoof, P. A. M. 2005, *ApJ*, 624, 794
- Shaw, G., Rawlins, K., & Srianand, R. 2016, *MNRAS*, 459, 3234
- Sofia, U. J., & Jenkins, E. B. 1998, *ApJ*, 499, 951
- Sonnentrucker, P., Friedman, S. D., & York, D. G. 2006, *ApJ*, 650, L115
- Steidel, C. C., & Sargent, W. L. W. 1992, *ApJS*, 80, 1
- Telikova, K. N., Balashev, S. A., Noterdaeme, P., Krogager, J. K., & Ranjan, A. 2020, *J. Phys. Conf. Ser.*, 1697, 012034
- Telikova, K. N., Balashev, S. A., Noterdaeme, P., Krogager, J. K., & Ranjan, A. 2022, *MNRAS*, 510, 5974
- Vernet, J., Dekker, H., D'Odorico, S., et al. 2011, *A&A*, 536, A105
- Wallström, S. H. J., Muller, S., Roueff, E., et al. 2019, *A&A*, 629, A128
- Welty, D. E., Sonnentrucker, P., Snow, T. P., & York, D. G. 2020, *ApJ*, 897, 36
- Werk, J. K., Rubin, K. H. R., Bish, H. V., et al. 2019, *ApJ*, 887, 89
- Wild, V., & Hewett, P. C. 2005, *MNRAS*, 361, L30
- Wild, V., Hewett, P. C., & Pettini, M. 2006, *MNRAS*, 367, 211
- Wolfe, A. M., Turnshek, D. A., Smith, H. E., & Cohen, R. D. 1986, *ApJS*, 61, 249
- Wolfe, A. M., Gawiser, E., & Prochaska, J. X. 2005, *ARA&A*, 43, 861
- Yèche, C., Palanque-Delabrouille, N., Claveau, C.-A., et al. 2020, *Res. Notes Am. Astron. Soc.*, 4, 179
- Zafar, T., Péroux, C., Popping, A., et al. 2013, *A&A*, 556, A141
- Zafar, T., Vladilo, G., Péroux, C., et al. 2014, *MNRAS*, 445, 2093
- Zou, S., Petitjean, P., Noterdaeme, P., et al. 2018, *A&A*, 616, A158
- Zych, B. J., Murphy, M. T., Hewett, P. C., & Prochaska, J. X. 2009, *MNRAS*, 392, 1429

Appendix A: Absorption line properties and figures*A.1. Details on abundance and kinematics of neutral gas ions and other fine structure transitions***Table A.1.** Column density (in logscale) of low ionisation gas species, N I, O I*, Ca II, S II, Na I P II, Ti II, Mn II, Ni II, and equivalent width (*w*) measurement of "Ca II λ 3934" and "Mg II λ 2803" for the ESDLAs sample.

QSO	$N(\text{N I})$	$N(\text{O I}^*)$	$N(\text{Ca II})$	$N(\text{S II})$	$N(\text{Na I})$	$w(\text{Ca II } \lambda 3934)$	$w(\text{Mg II } \lambda 2803)$	$N(\text{P II})$	$N(\text{Ti II})$	$N(\text{Mn II})$	$N(\text{Ni II})$
J0017+1307	16.53±0.23	<13.30	13.22±0.33	B	<13.53	0.34±0.04	2.22±0.03	-	~13	13.1±0.1	14.1±0.1
J0025+1145	-	<15.26	12.94±0.02	>16.4	-	0.36±0.02	4.2±0.01	-	13.31±0.04	14.00±0.01	14.88±0.02
J1143+1420	<15.7	<19.16	<13.19	B	<13.65	<0.68	4.08±0.08	-	~13.68	13.59±0.01	14.53±0.02
J1258+1212	<16.25	<14.12	-	~15.40	<11.96	0.72±0.07	1.90±0.02	-	13.1±0.2	13.1±0.1	14.0±0.1
J1349+0448	-	<13.87	-	B	<13.48	0.92±0.13	2.13±0.07	-	~13.3	13.35±0.04	14.4±0.1
J1411+1229	15.52±0.11	~13.42	-	B	<15.03	1.23±0.09	0.53±0.05	13.9±0.7	~12.9	13.2±0.1	14.2±0.1
J1513+0352	-	<14.70	~12.3	B	<12.79	<0.13	2.84±0.04	-	~12.8	-	14.1±0.1
J2140-0321	15.75±0.11	13.82±0.1	12.71±0.1	15.61±0.07	<12.83	0.13±0.03	1.31±0.01	15.5±0.7	13.2±0.1	13.51±0.02	14.35±0.06
J2232+1242	15.5±0.11	~13.46	<12.57	15.49±0.01	<12.76	0.18±0.03	1.98±0.01	14.1±0.1	13.1±0.1	13.23±0.01	14.26±0.02
J2246+1328	<13.87	<13.22	~12.85	15.16±0.27	<13.45	<0.38	0.72±0.01	13.4±0.1	<12.7	12.96±0.05	13.7±0.1
J2322+0033	<15.24	<13.59	-	14.63±0.07	<11.39	<0.70	1.50±0.04	-	~13.2	12.93±0.05	13.83±0.05

Notes. Symbol 'B' means that all the transition lines for that species are blended and hence the column density cannot be estimated.

A.2. Absorption line figures

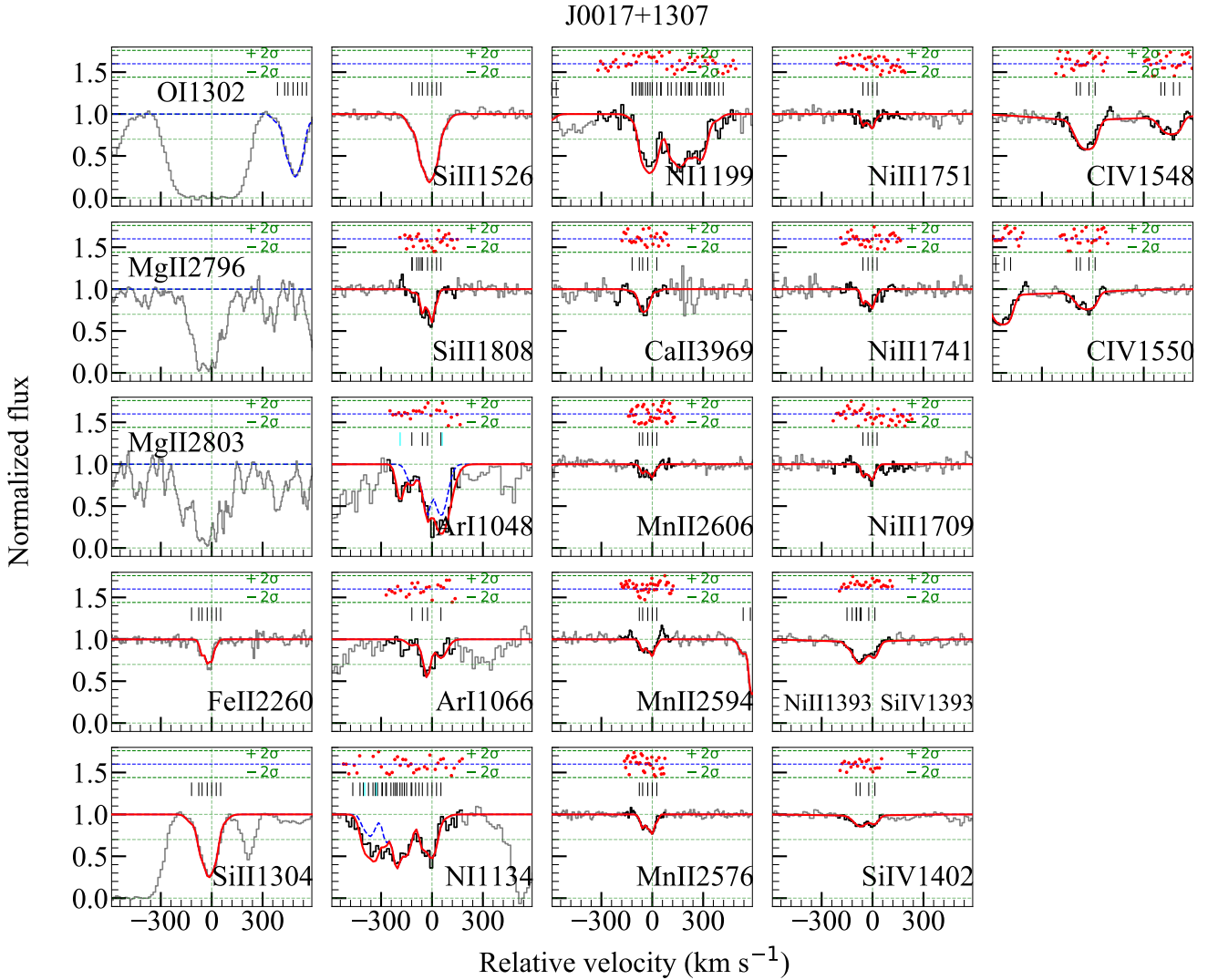


Fig. A.1. Different ionisation metal lines (O I, Mg II, Fe II, Si II, Ar I, Ni I, Ca II, Mn II, Ni II, Si IV, and C IV) associated with the $z_{\text{abs}} = 2.326$ ESDLA system towards QSO SDSS J0017+1307. The normalised X-shooter spectrum is shown in grey, the continuum is shown as a dashed green line, with the total best-fit multi-component Voigt profile over-plotted in red. The highlighted part of the spectrum (in black) shows the data that were used to constrain the fit. The residuals are shown above each line in areas used for the fit in units of the standard deviation ($\pm 2\sigma$) from the error spectrum. In some of the plots where there is contamination either from the Ly α forest or from other transitions from different absorber systems, apart from the total modelled profile in red, the modelled profile for the labelled transition is also shown as a dashed blue line. Short vertical marks (or ticks) in black show the location of the different velocity components. The position of blends with the Ly α forest and other absorption systems unrelated to the ESDLA are shown with cyan ticks. There is a velocity shift between the UVB and the VIS arm spectra for some systems (see [Ranjan et al. 2020](#), for more details). The velocity shifted positions, if any, are indicated with magenta ticks. The sub-component redshifts and b -values of neutral and singly ionised gas species, such as Ar I, Ni I, and Ca II, are tied together. The sub-component redshifts and b -values for Si IV and C IV profiles are also tied together. The saturated absorption profiles for O I and Mg II are shown for reference. The subplot with Fe II is taken from [Ranjan et al. \(2020\)](#) and is shown here just for reference.

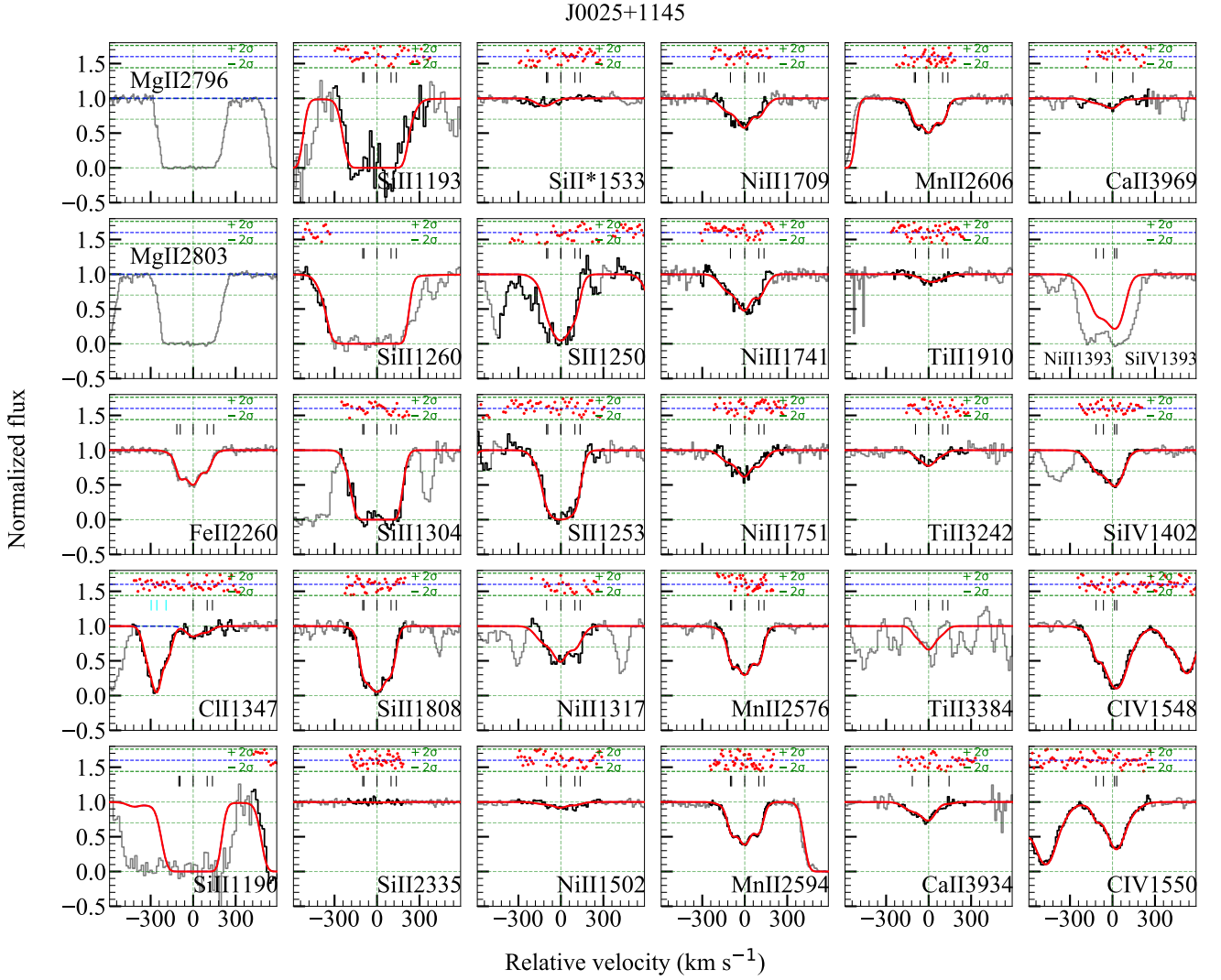


Fig. A.2. Different ionisation metal lines (O I, Mg II, Cl I, Fe II, Si II, S II, Ni II, Mn II, Ti II, Ca II, Si IV, and C IV) associated with the $z_{\text{abs}} = 2.304$ ESDLA system towards QSO SDSS J0025+1145. The legends as well as the assumption on sub-component redshifts and b -values are the same as in Fig. A.1.

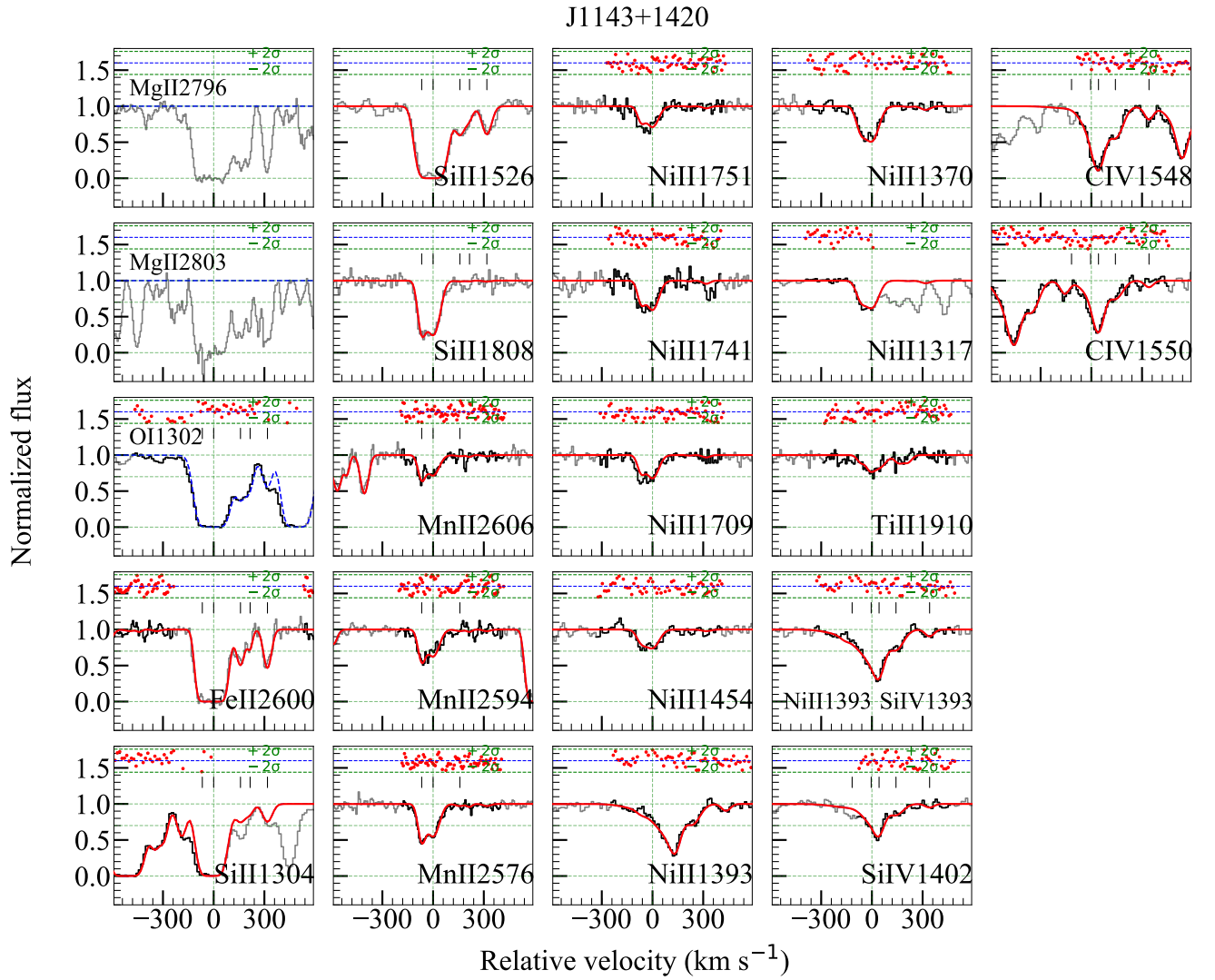


Fig. A.3. Different ionisation metal lines (Mg II, O I, Fe II, Si II, Mn II, Ni II, Ti II, Si IV, and C IV) associated with the $z_{\text{abs}} = 2.323$ ESDLA system towards QSO SDSS J1143+1420. The legends as well as the assumption on sub-component redshifts and b -values are the same as in Fig. A.1.

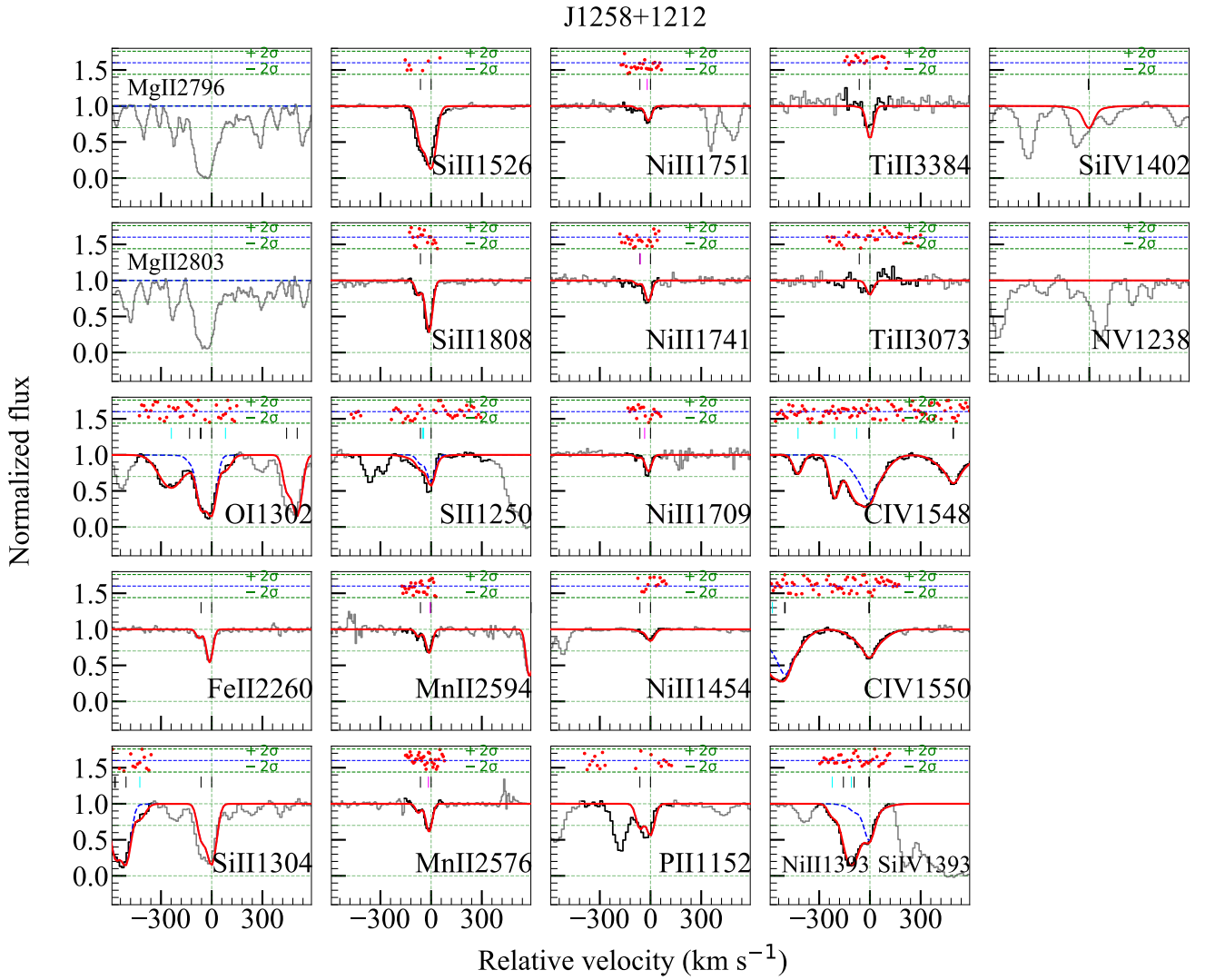


Fig. A.4. Different ionisation metal lines (Mg II, O I, Fe II, Si II, S II, Mn II, Ni II, P II, Ti II, C IV, Si IV, and N V) associated with the $z_{\text{abs}} = 2.444$ ESDLA system towards QSO SDSS J1258+1212. We note that N V transitions are heavily contaminated with the Ly α forest and hence we could not find any robust solution for the column density tied with C IV. Hence, we only show the spectrum of "N V λ 1238" here without the fit. The legends as well as the assumption on sub-component redshifts and b -values are the same as in Fig. A.1.

J1349+0448

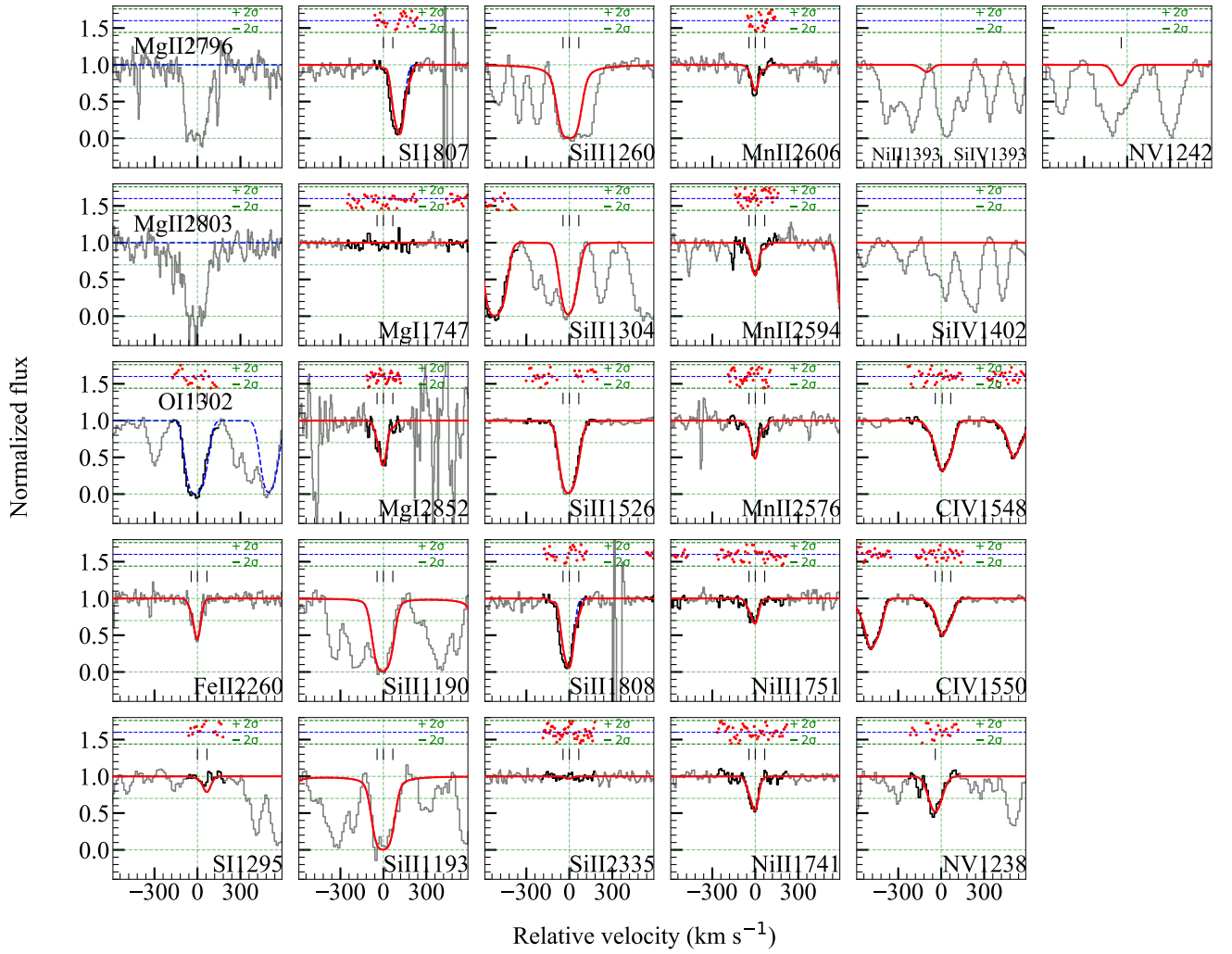


Fig. A.5. Different ionisation metal lines (Mg II, O I, Fe II, Si II, Mn II, Ni II, Si IV, C IV, and N V) associated with the $z_{\text{abs}} = 2.482$ ESDLA system towards QSO SDSS J1349+0448. The sub-component redshifts and b -values of C IV and N V are also tied together. 'N V $\lambda 1242$ ' is contaminated and hence the transition was not used for fitting. The Si IV profiles are strongly blended and we could not find any robust solution for the column density tied with C IV. Here, we just show the unfitted spectrum for reference. The cyan tick in the 'Si II $\lambda 1526$ ' subplot represents a blend with an Mg II absorption system at $z_{\text{abs}} = 0.8998$. The legends as well as the assumption on sub-component redshifts and b -values are the same as in Fig. A.1.

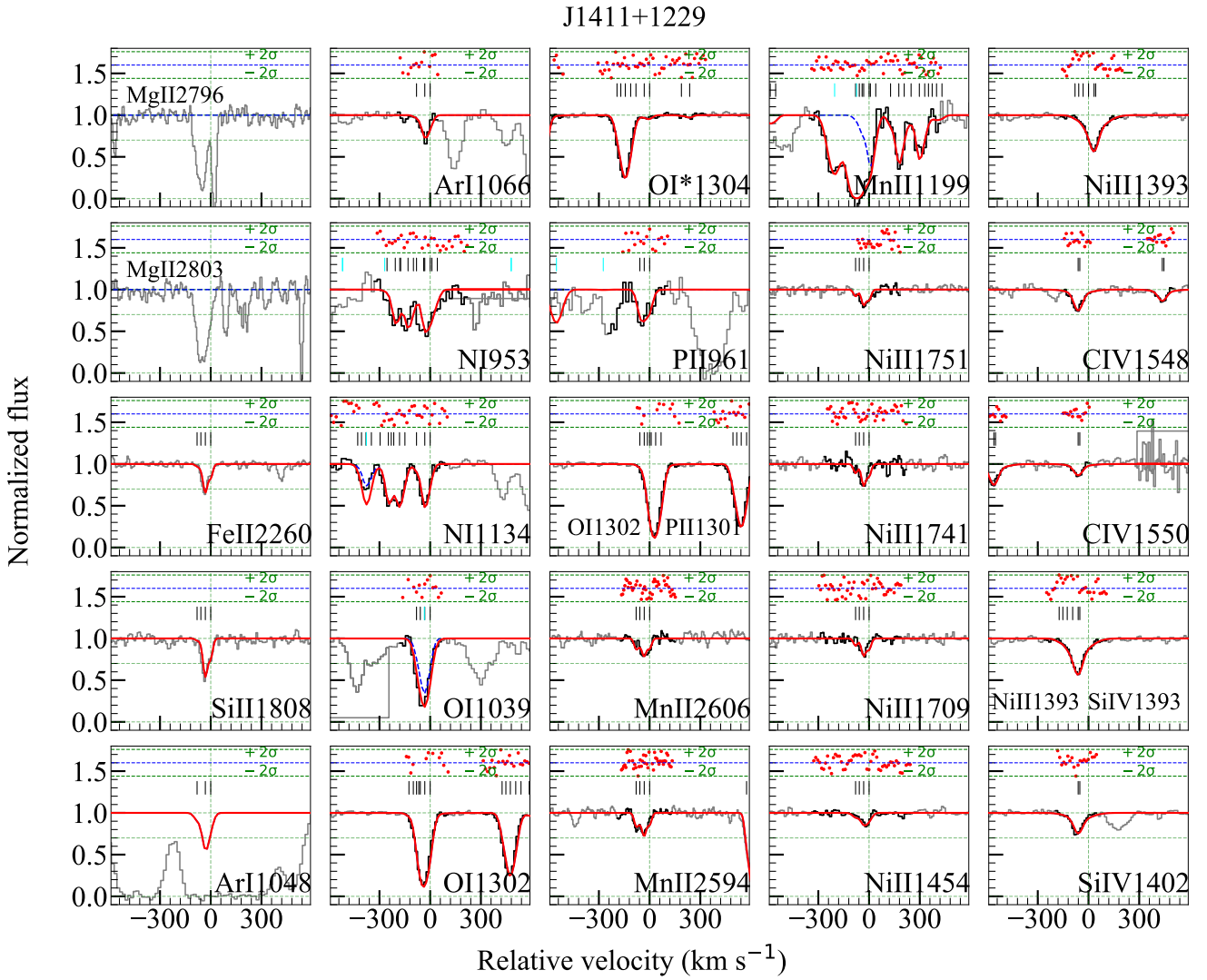


Fig. A.6. Different ionisation metal lines (Mg II, Fe II, Si II, Ar I, Ni I, O I, O I*, P II, Mn II, Ni II, C IV, and Si IV) associated with the $z_{\text{abs}} = 2.545$ ESDLA system towards QSO SDSS J1411+1229. The subplot with 'Ar I1048' shows the mock Ar I profile on top of the spectrum, heavily contaminated with the Ly α forest and it was not used for fitting. The legends as well as the assumption on sub-component redshifts and b -values are the same as in Fig. A.1.

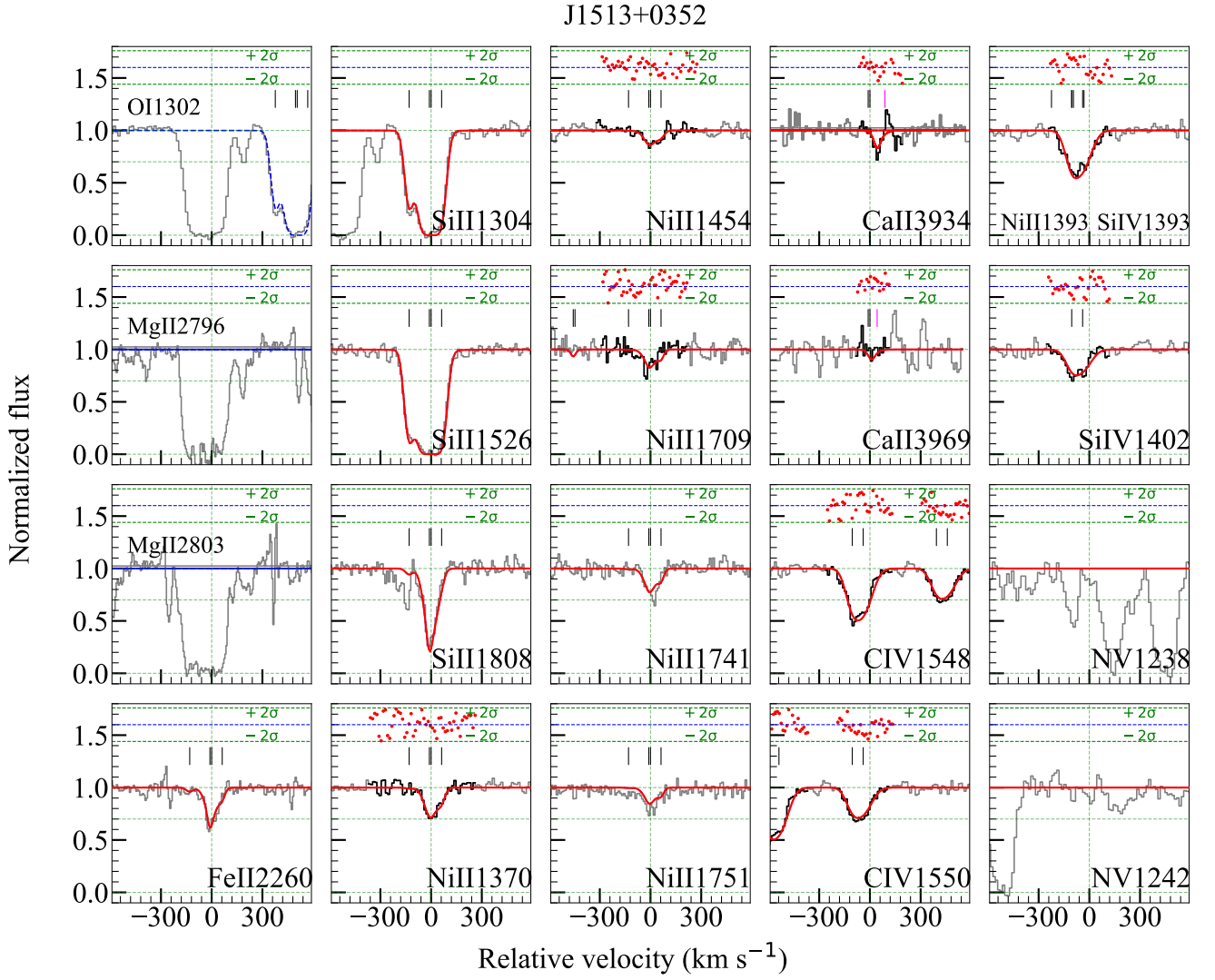


Fig. A.7. Different ionisation metal lines (OI, Mg II, Fe II, Si II, Ni II, Ca II, C IV, and NV) associated with the $z_{\text{abs}} = 2.464$ ESDLA system towards QSO SDSS J1513+0352. The NV transitions are heavily contaminated with the Ly α forest and hence we could not find any robust solution for the column density tied with C IV. Hence, we only show the NV absorption profiles here without the fit. The legends as well as the assumption on sub-component redshifts and b -values are the same as in Fig. A.1.

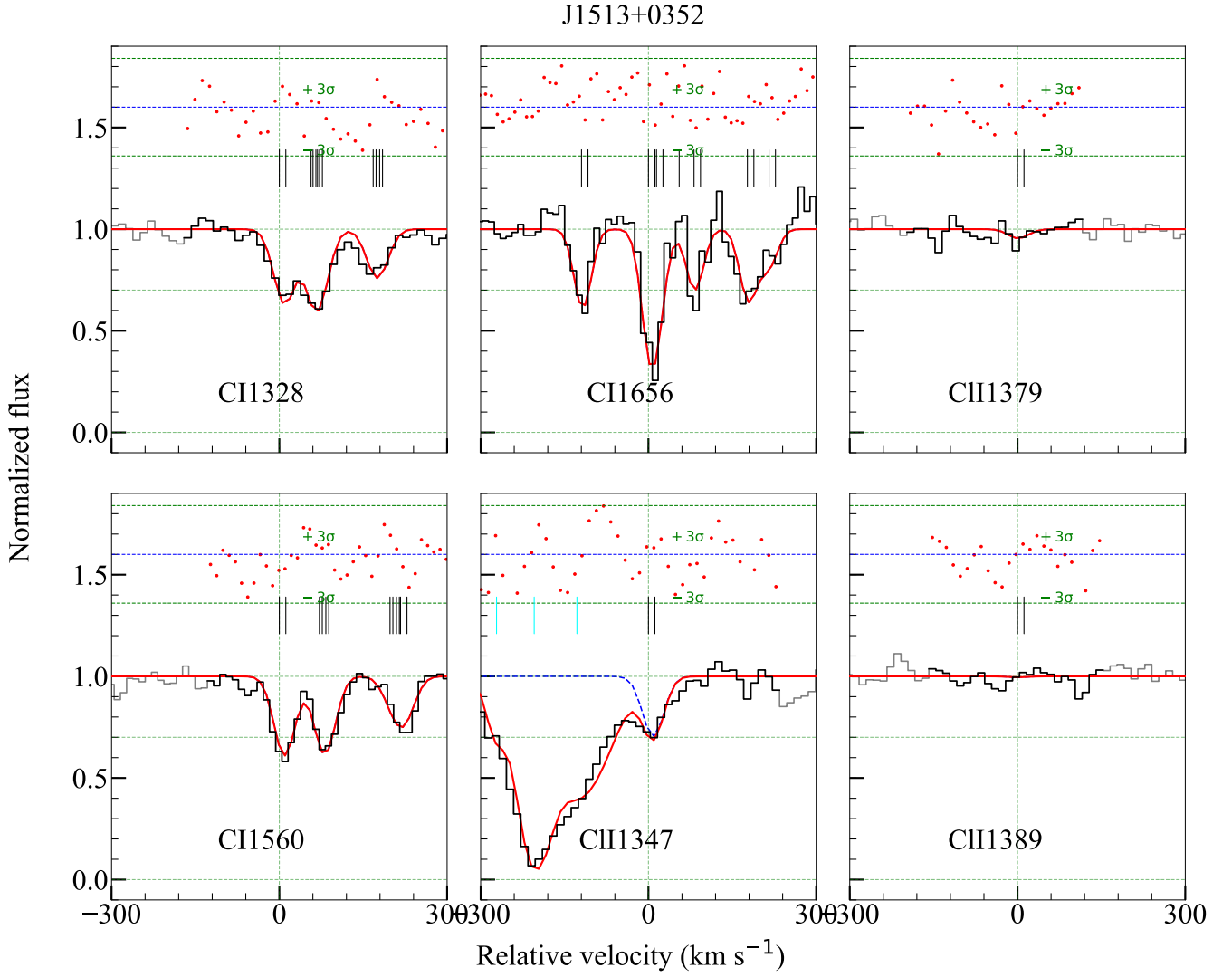


Fig. A.8. Fit to C I and C II lines associated with the $z_{\text{abs}} = 2.464$ ESDLA system towards QSO SDSS J1513+0352. The plot with neutral chlorine ('C II $\lambda 1347$ ' transition) includes velocity components from two other absorption systems, $z_{\text{abs}} = 2.339$ (Si IV absorber) and $z_{\text{abs}} = 2.006$ (C IV absorber), fitted together. The total C I column density ($\log N(\text{C I}) = 15.2 \pm 0.8$, $\log N(\text{C I}^*) = 15.0 \pm 0.8$ and $\log N(\text{C I}^{**}) = 14.6 \pm 0.7$) with a multi-component fit is consistent with the single component fit result reported in [Ranjan et al. \(2018\)](#).

J2140-0321

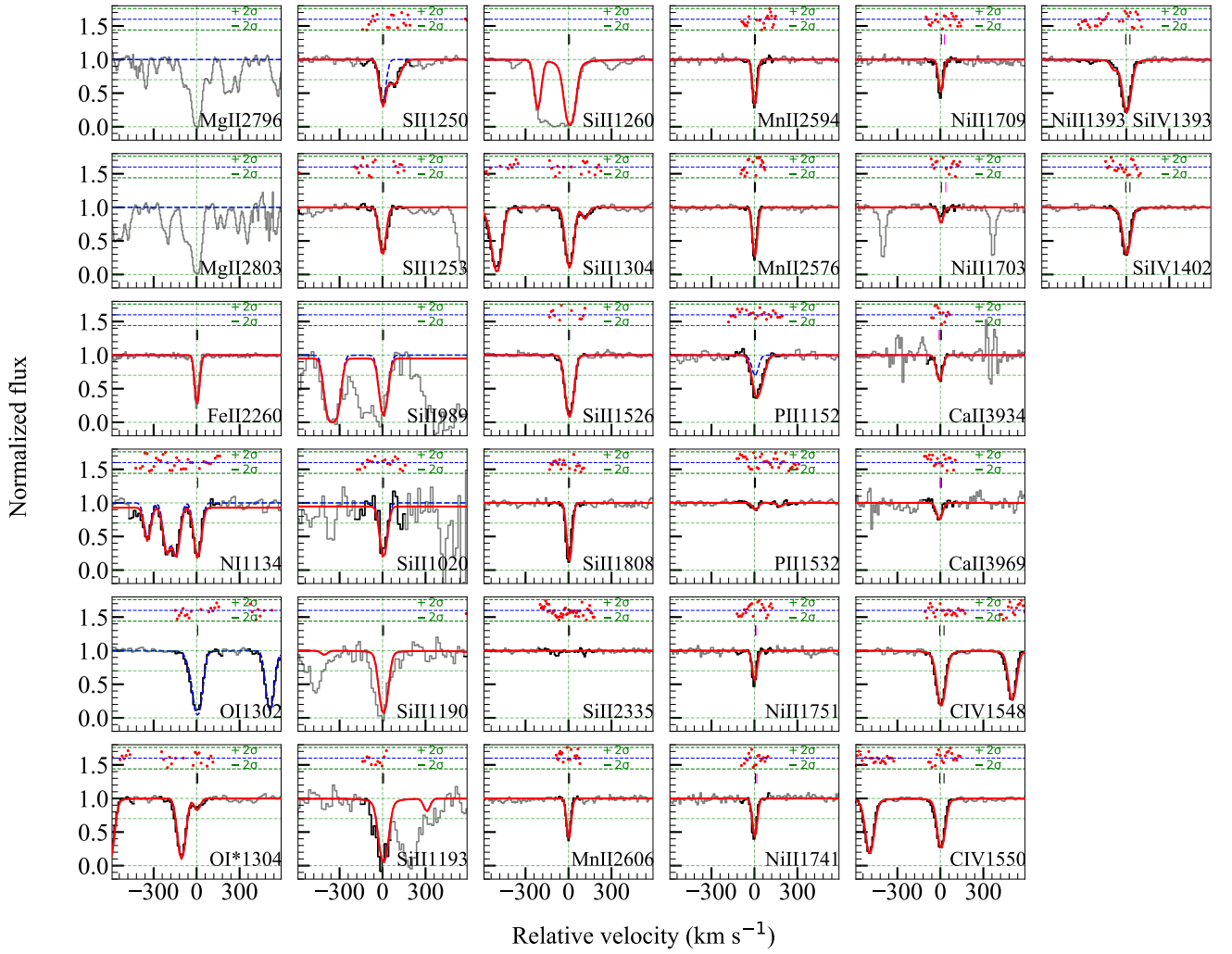


Fig. A.9. Different ionisation metal lines (Mg II, Fe II, Si II, Ni I, O I, O I*, S II, Mn II, P II, Ni II, Ca II, C IV, and Si IV) associated with the $z_{\text{abs}} = 2.339$ ESDLA system towards QSO SDSS J2140–0321. The plots showing 'O I $\lambda 1302$ ' and 'O I* $\lambda 1304$ ' include additional components from 'Si II $\lambda 1304$ ' transition. The legends as well as the assumption on sub-component redshifts and b -values are the same as in Fig. A.1.

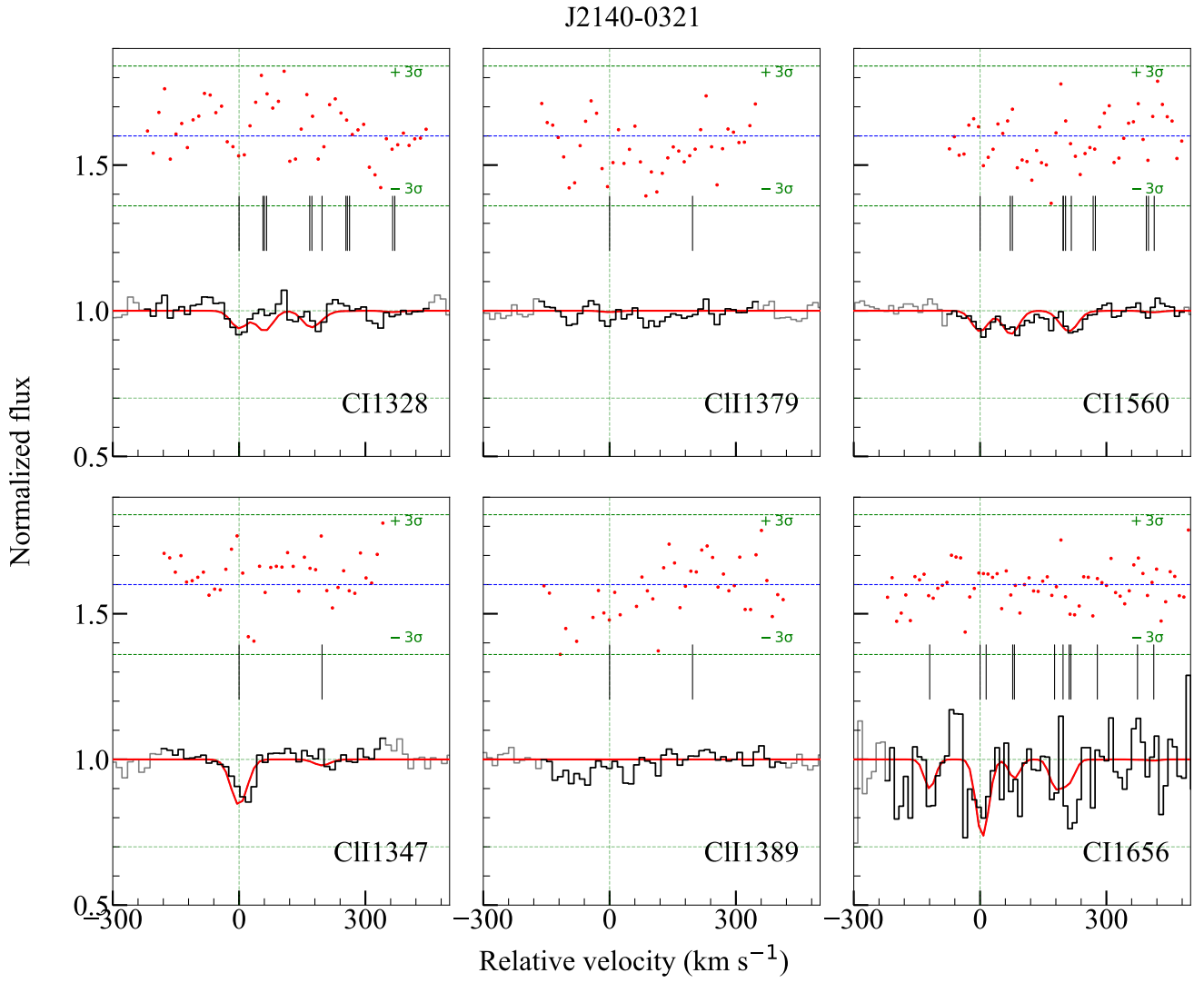


Fig. A.10. Fit to C I and C II lines associated with the $z_{\text{abs}} = 2.339$ ESDLA system towards QSO SDSS J2140–0321. The total C I column density ($\log N(\text{C I}) = 13.18 \pm 0.04$) with a multi-component fit is ~ 0.3 dex smaller than the single component fit result reported in [Ranjan et al. \(2020\)](#)

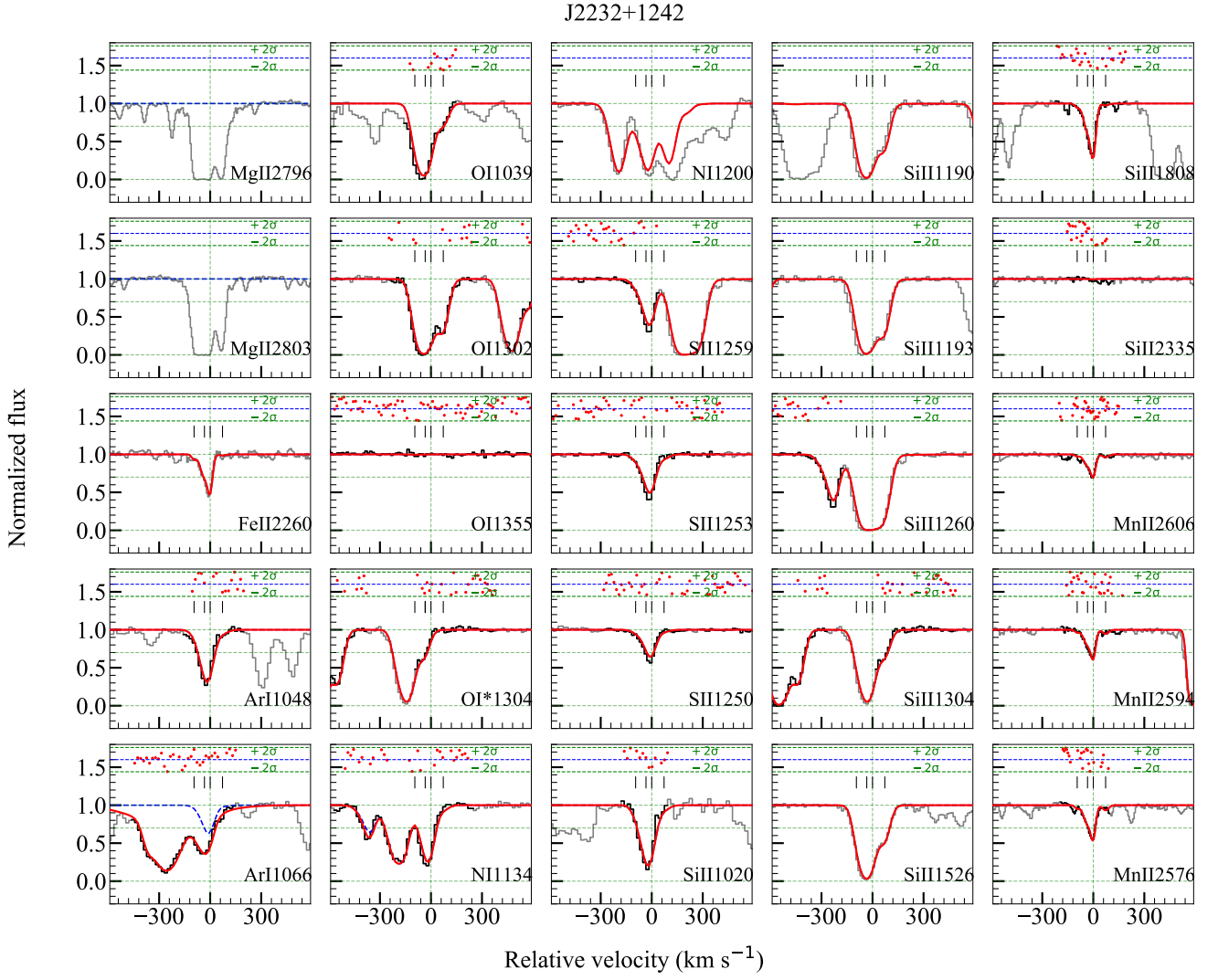


Fig. A.11. Different ionisation metal lines (Mg II, Fe II, Ar I, O I, O I*, N I, S II, Si II, and Mn II) associated with the $z_{\text{abs}} = 2.230$ ESDLA system towards QSO SDSS J2232+1242. The plots show 'O I $\lambda 1302$ ' and 'O I* $\lambda 1304$ '. The subplots showing 'Ar I $\lambda 1066$ ' and 'N I $\lambda 1134$ ' transitions have contamination from the Ly α forest that were included while fitting. The legends as well as the assumption on sub-component redshifts and b -values are the same as in Fig. A.1.

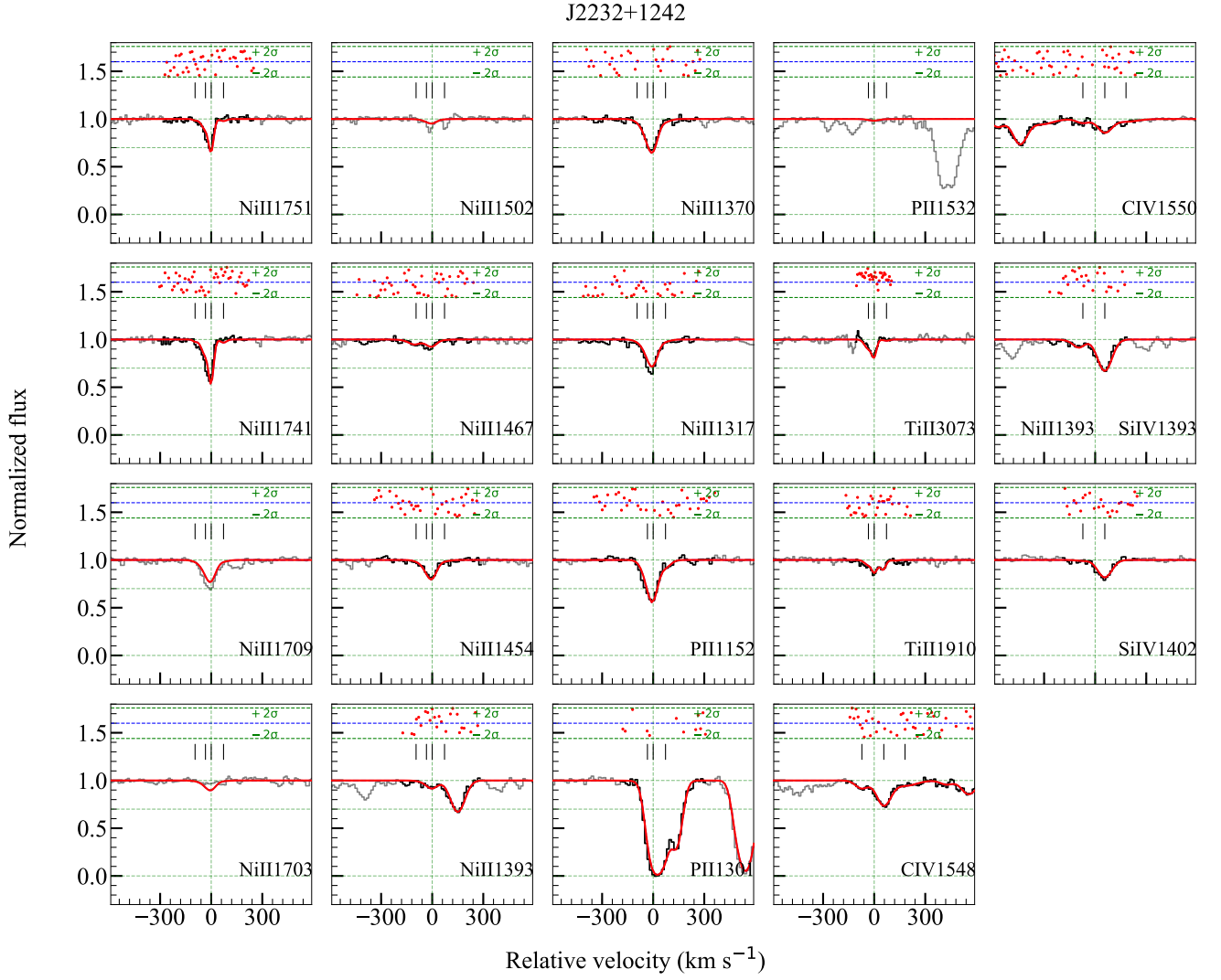


Fig. A.12. Different ionisation metal lines (Ni II, P II, Ti II, C IV, and Si IV) associated with the $z_{\text{abs}} = 2.230$ ESDLA system towards QSO SDSS J2232+1242. The legends as well as the assumption on sub-component redshifts and b -values are the same as in Fig. A.1.

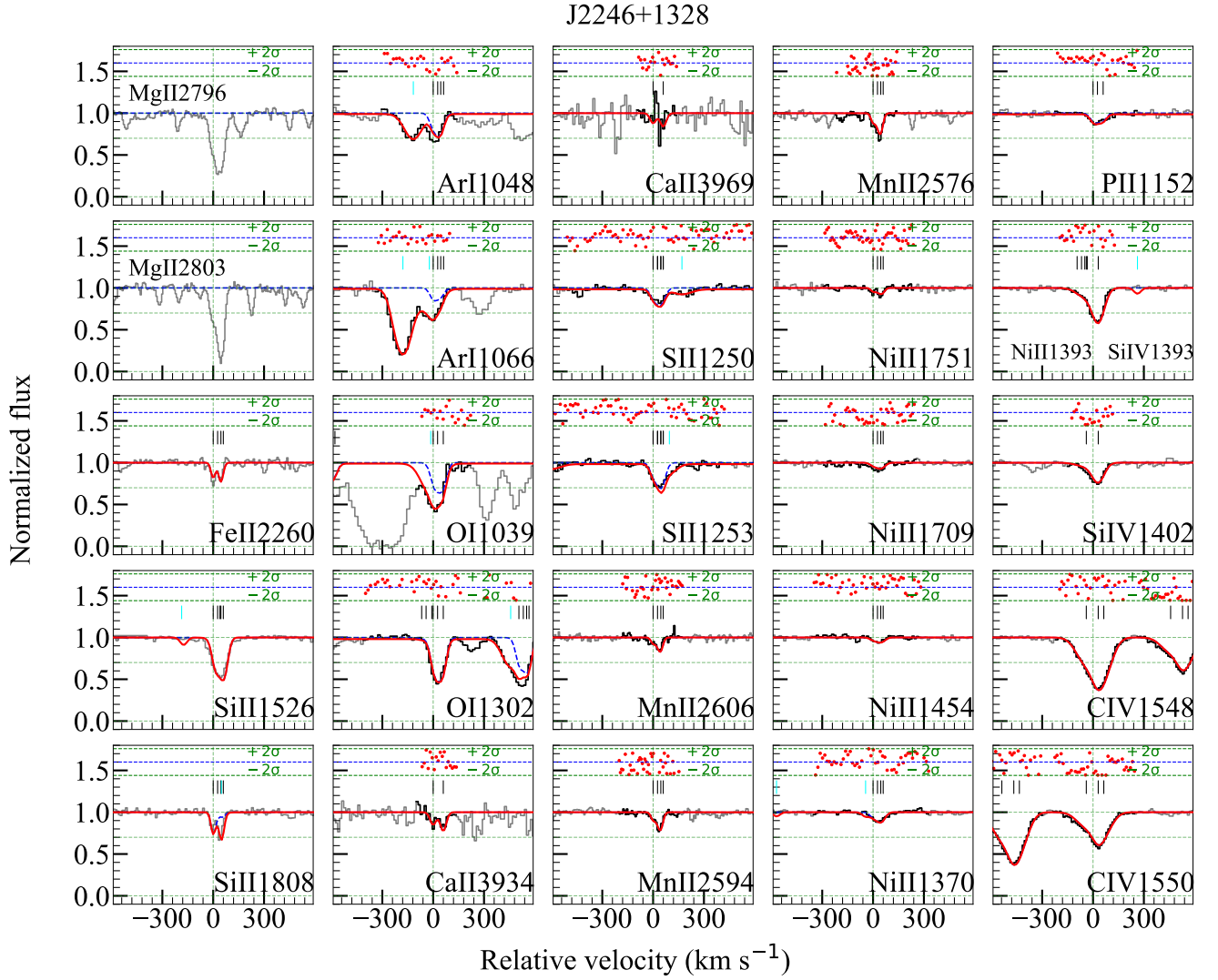


Fig. A.13. Different ionisation metal lines (Mg II, Fe II, Si II, Ar I, O I, Ca II, S II, Mn II, Ni II, P II, Si IV, and C IV) associated with the $z_{\text{abs}} = 2.215$ ESDLA system towards QSO SDSS J2246+1328. The plots with neutral argon (Ar I) includes components from the Ly α forest (H I) lines. The legends as well as the assumption on sub-component redshifts and b -values are the same as in Fig. A.1.

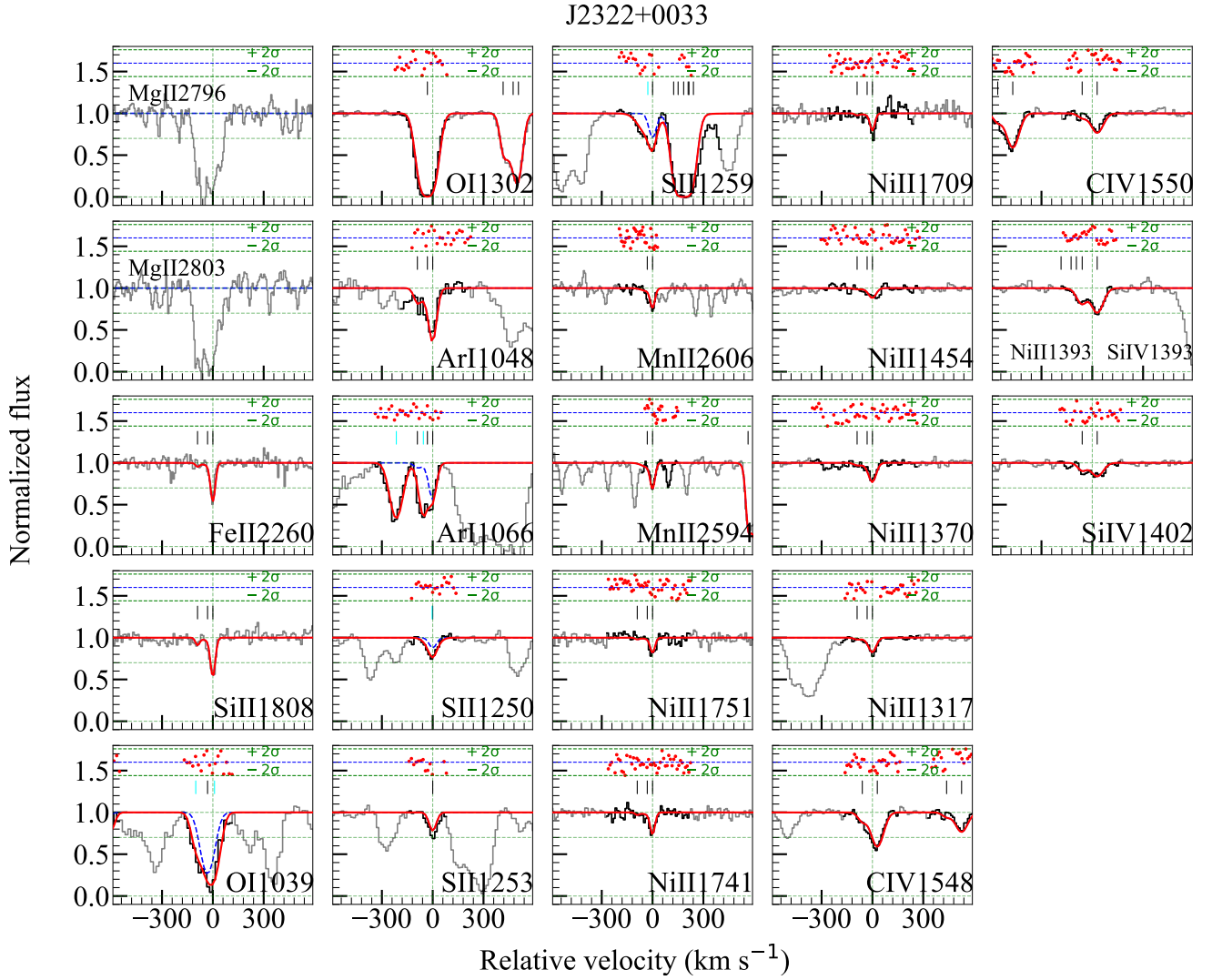


Fig. A.14. Different ionisation metal lines (Mg II, Fe II, Si II, O I, Ar I, S II, Mn II, Ni II, C IV, and Si IV) associated with the $z_{\text{abs}} = 2.477$ ESDLA system towards QSO SDSS J2322+0033. The legends as well as the assumption on sub-component redshifts and b -values are the same as in Fig. A.1.